Journal of Clinical and Translational Hepatology **2026** vol. 14(4) | 399–415
DOI: 10.14218/JCTH.2025.00561

Original Article

Galectin-3 Promotes Graft Injury via NLRP3 Pyroptosis in Steatotic Liver Transplantation: A Therapeutic Target for Donor Optimization

Xianwu Yang[1#], Shirui Huang[1#], Ruisi Ma[1], Zhihui Zhu[2], Yingquan Zhuo[1], Jiafei Yang[1], Jun Du[1*] and Huajian Gu[1*]

[1]Department of Pediatric Surgery, Affiliated Hospital of Guizhou Medical University, Guiyang, Guizhou, China; [2]Department of Pediatric Urology, Guiyang Maternal and Child Health Care Hospital, Guiyang, Guizhou, China

Received: October 24, 2025 | **Revised:** January 13, 2026 | **Accepted:** February 03, 2026 | **Published online:** March 24, 2026

Abstract

Background and Aims: Steatotic donor livers are highly susceptible to post-transplant dysfunction; however, the underlying mechanisms remain incompletely understood. This study aimed to investigate the role of galectin-3 (LGALS3)-mediated pyroptosis in steatotic liver graft injury and explore its therapeutic potential. ***Methods:*** A mouse model of steatotic liver transplantation was established. Graft tissues were subjected to RNA sequencing to identify key regulators. *In vitro*, LGALS3 was modulated in steatotic hepatocytes under ischemia/reperfusion stress to assess its impact on the NLRP3 inflammasome and pyroptosis. The regulatory mechanism by which LGALS3 modulates NLRP3 ubiquitination was further examined. Finally, the therapeutic efficacy of LGALS3 inhibition was evaluated in an orthotopic liver transplantation model. ***Results:*** Transcriptomic analysis identified LGALS3 as a key upregulated molecule in steatotic grafts, associated with pyroptosis pathways. *In vitro*, LGALS3 overexpression enhanced NLRP3 inflammasome activation and pyroptotic cell death, whereas LGALS3 knockdown exerted protective effects. Mechanistically, LGALS3 modulated NLRP3 inflammasome activity by regulating its ubiquitination. *In vivo*, pharmacological inhibition of LGALS3 significantly improved graft function, reduced histological injury, suppressed pyroptosis, and prolonged recipient survival. ***Conclusions:*** This study demonstrates that LGALS3 drives steatotic graft injury by promoting NLRP3-mediated pyroptosis through the regulation of ubiquitination. These findings identify LGALS3 as a promising target for improving the outcomes of liver transplantation using steatotic donor organs.

Citation of this article: Yang X, Huang S, Ma R, Zhu Z, Zhuo Y, Yang J, *et al*. Galectin-3 Promotes Graft Injury via NLRP3 Pyroptosis in Steatotic Liver Transplantation: A Therapeutic Target for Donor Optimization. J Clin Transl Hepatol 2026;14(4):399–415. doi: 10.14218/JCTH.2025.00561.

Introduction

Non-alcoholic fatty liver disease (NAFLD) has become the most prevalent chronic liver condition worldwide, encompassing a broad disease spectrum ranging from simple hepatic steatosis with or without mild inflammation (non-alcoholic fatty liver) to non-alcoholic steatohepatitis (NASH).[1,2] Over the past two decades, the global incidence of NAFLD has risen steadily and is projected to make it one of the leading causes of end-stage liver disease and hepatic failure in the coming decades.[3–5]

Liver transplantation remains the only effective treatment for end-stage liver disease, and the proportion of NAFLD-related cirrhosis among transplant indications continues to rise.[6] However, compared with non-steatotic grafts, steatotic livers are markedly more susceptible to ischemia/reperfusion (I/R) injury and are at higher risk of developing primary graft dysfunction after transplantation.[7] This dysfunction is characterized by an exacerbated early inflammatory response, hepatocellular necrosis, and delayed functional recovery.[8,9] Consequently, graft steatosis has become a major clinical obstacle that compromises post-transplant prognosis in patients with NAFLD. Although the macroscopic pathological features of steatotic liver grafts have been extensively described, the molecular mechanisms underlying post-transplant dysfunction remain poorly defined. In particular, the regulatory processes governing cell death pathways and immune–inflammatory responses are incompletely understood. Therefore, elucidating the key regulatory events during the functional recovery of steatotic liver grafts is of significant clinical value for improving graft quality and post-transplant outcomes.

Programmed cell death, as a central biological process regulating tissue homeostasis and stress response, plays a pivotal role in the pathological changes that occur after liver transplantation.[10,11] Among the various forms of programmed cell death, pyroptosis has attracted increasing attention under complex stress conditions such as steatotic liver disease,

---

Keywords: Galectin-3; Pyroptosis; NLRP3 Inflammasome; Liver Transplantation; Fatty Liver; Ischemia-Reperfusion Injury; Ubiquitination; Inflammation; Hepatocytes.

[#] Contributed equally to this work.

[*] **Correspondence to:** Huajian Gu and Jun Du, Department of Pediatric Surgery, Affiliated Hospital of Guizhou Medical University, 28 Guiyi Street, Yunyan District, Guiyang, Guizhou 550004, China. ORCID: https://orcid.org/0009-0000-6658-4991 (HG) and https://orcid.org/0009-0000-8499-1312 (JD). Tel: +86-851-86855119, Fax: +86-851-86855119, E-mail: guhuajian_wh@163.com (HJG) and 1091766237@qq.com (JD).

I/R injury, and organ transplantation, owing to its highly proinflammatory nature.[12,13] As an inflammatory form of programmed cell death, pyroptosis is closely associated with the initiation and progression of NAFLD, primarily through the release of pro-inflammatory cytokines (e.g., IL-1β and IL-18), which further amplify local inflammatory responses and accelerate pathological progression. During NAFLD development, multiple factors, including lipotoxic stress, innate immune activation, endoplasmic reticulum stress, gut microbiota dysbiosis, and oxidative stress, interact synergistically to drive the transition from simple hepatic steatosis to NASH and ultimately cirrhosis.[14] Pyroptosis is mainly mediated by the NLRP3 inflammasome, which activates caspase-1 to cleave gasdermin D (GSDMD), thereby inducing membrane pore formation, cellular content release, and robust local inflammatory responses, accompanied by the secretion of mature IL-1β and IL-18.[15,16] Previous studies have shown that the NLRP3–IL-1β–NF-κB signaling axis is aberrantly activated during hepatic I/R injury and steatotic liver progression, serving as a critical pathway that induces hepatocyte pyroptosis, promotes localized immune inflammation, and impairs tissue repair.[12,17] However, in the context of steatotic liver transplantation, the dynamic regulatory mechanisms of NLRP3 inflammasome activity remain unclear. In particular, how upstream molecules modulate its activation to influence post-transplant pyroptosis levels and liver function recovery has not been thoroughly investigated. Defining the spatiotemporal dynamics of pyroptosis in steatotic liver grafts and identifying its key regulatory factors will provide a theoretical foundation for developing novel therapeutic strategies.

RNA-binding proteins (RBPs) exert essential post-transcriptional regulatory functions in a wide range of physiological and pathological processes, including mRNA stability, alternative splicing, and translational control.[18,19] In recent years, certain RBPs have been identified to possess multifaceted capabilities in modulating forms of cell death, immune–inflammatory responses, and ubiquitination.[20,21] Galectin-3 (LGALS3), a prototypical RBP, is highly expressed in multiple liver disease models. Beyond its role in modulating mRNA stability, LGALS3 participates in the activation of inflammatory pathways and the regulation of protein ubiquitination.[22,23] Evidence has shown that LGALS3 plays a pivotal role in hepatic I/R injury, steatosis, and fibrosis.[24–26] However, whether LGALS3 contributes to functional recovery after steatotic liver graft transplantation by modulating the pyroptosis signaling axis remains unclear. Notably, ubiquitination, a central mechanism governing protein degradation, signal transduction, and inflammatory responses, has been shown to critically regulate both the assembly and inactivation of the NLRP3 inflammasome.[27–29] Previous studies have suggested that LGALS3 may act as a regulatory component of E3 ligase complexes, thereby influencing the ubiquitination status of NLRP3 and modulating its activity and downstream pyroptotic signaling.[30,31] Nevertheless, the molecular link between LGALS3 and the ubiquitination of NLRP3 has not yet been systematically elucidated.

Using both a murine steatotic liver transplantation model and a human hepatocyte steatosis model, combined with genetic manipulation and small-molecule inhibitors, the role of LGALS3 in regulating the NLRP3–IL-1β–NF-κB pyroptosis pathway was investigated both *in vivo* and *in vitro*. This integrated approach enabled the evaluation of its effects on postoperative inflammatory responses, liver function recovery, and tissue regeneration. Accordingly, elucidating the molecular mechanisms by which LGALS3 regulates pyroptosis through ubiquitination provides important mechanistic insights and holds substantial translational potential.

This study aimed to systematically investigate the regulatory mechanisms of the NLRP3–IL-1β–NF-κB pyroptosis pathway mediated by the RBP LGALS3 through RNA sequencing (RNA-seq), with a particular focus on its pivotal role in inflammatory pyroptosis following steatotic liver graft transplantation. Using a murine orthotopic steatotic liver transplantation model and a human hepatocyte steatosis model, we validated the molecular mechanism by which LGALS3 modulates NLRP3 activity and its downstream pyroptotic signaling via regulation of NLRP3 ubiquitination. We also explored the effects of LGALS3 inhibition on post-transplant liver function recovery and assessed its therapeutic potential. The study is expected to reveal a novel molecular mechanism underlying the regulation of pyroptosis in steatotic liver grafts after transplantation, thereby identifying LGALS3 as an upstream modulator of the NLRP3–IL-1β–NF-κB axis. These findings provide a theoretical foundation and potential therapeutic target for improving graft quality and post-transplant prognosis in the context of NAFLD. Moreover, this research expands the current understanding of RBPs in hepatic stress responses and offers new insights for the development of targeted therapeutic strategies.

Methods

Ethics statement

This study strictly adhered to all relevant ethical guidelines and regulations concerning animal experimentation. All procedures were approved by the Institutional Animal Care and Use Committee of the Affiliated Hospital of Guizhou Medical University (2024-729). Animals were housed and handled under humane conditions, and every effort was made to minimize pain and distress. At the conclusion of the experiments, all animals were humanely euthanized under ether anesthesia.

The use of human liver samples was approved by the Ethics Committee of the Affiliated Hospital of Guizhou Medical University (2022-52). All procedures conformed to the principles of the Declaration of Helsinki and relevant national regulations. Written informed consent was obtained from all organ donors or their legal representatives prior to sample collection. All donor livers were procured through the China Organ Transplant Response System, and no organs were obtained from executed prisoners. Donor anonymity was strictly maintained throughout the study, and all samples were used exclusively for scientific research.

Human liver samples

Pre-reperfusion liver specimens were collected from the cold-stored left lobe immediately before transplantation. Post-reperfusion samples were obtained from the same lobe 2 h after portal vein reperfusion, immediately prior to abdominal closure. Specimens were either fixed in formalin for histopathological analysis, snap-frozen in liquid nitrogen for immunoblotting assays, or preserved in University of Wisconsin cold storage solution and subsequently transported to the laboratory for primary hepatocyte isolation. All donor livers were procured through the China Organ Transplant Response System between August 2022 and October 2023. Hepatic steatosis was independently assessed by two experienced pathologists, with steatosis defined as macrovesicular fat involvement greater than 5%. A total of 45 normal donor livers and 45 steatotic donor livers from donation after circulatory death were enrolled in this study. Baseline characteristics of donors and recipients are provided in Supplementary Tables 1 and 2.

Animal models and tissue sample collection

Eight- to ten-week-old male BALB/c mice (SPF grade; 20–25 g) were obtained from Beijing Vital River Laboratory Animal Technology Co., Ltd. (License No. SCXK(Beijing)2016-0006). Animals were housed in an SPF facility under controlled conditions (12 h light/dark cycle, 22 ± 2 °C, 50 ± 5% humidity), with ad libitum access to food and water. Mice were randomly assigned to five groups (n = 15 per group): Sham, Fat + Tx, Fat + Tx + siLGALS3, Fat + Tx + ML265, and Fat + Tx + ML265 + MCC950. Except for the Sham group, all mice were fed a high-fat diet (HFD, 60% kcal from fat, Research Diets, D12492) for 12 consecutive weeks to induce hepatic steatosis. At the end of the 12th week, a subset of mice (n = 3) was randomly selected for euthanasia, and liver tissues were harvested for hematoxylin and eosin (H&E) staining (Solarbio, G1120) and Oil Red O staining (Sigma-Aldrich, O0625) to confirm steatosis and evaluate morphological alterations. Following model validation, semi-orthotopic liver transplantation was performed using standard microvascular anastomosis techniques (Kamada method).[32] In donor mice, the portal vein, hepatic artery, and bile duct were carefully isolated and anastomosed to corresponding recipient structures to re-establish vascular and biliary continuity and restore hepatic perfusion. During surgery, the recipient's body temperature and hemodynamic status were continuously monitored using a small animal heating pad (Harvard Apparatus, 507222F) to ensure intraoperative stability and postoperative recovery. Mice in the Sham group underwent laparotomy with exposure of the hepatic hilum without liver transplantation, serving as surgical controls.

Interventions were administered according to group allocation. In the Fat + Tx + siLGALS3 group, LGALS3 knockdown (shLGALS3) was achieved by tail vein injection of siLGALS3 lentiviral particles (1 × 10^9 PFU/mouse; GeneChem, Shanghai; LV-hLGALS3-shRNA) three days before surgery. Knockdown efficiency was confirmed at the time of transplantation using reverse transcription quantitative PCR (RT-qPCR). In the Fat + Tx + ML265 group, mice received an intraperitoneal injection of ML265 (a LGALS3 inhibitor; 10 mg/kg; MedChemExpress, HY-112002, dissolved in saline) one day before and 6 h after transplantation. In the Fat + Tx + ML265 + MCC950 group, MCC950 (an NLRP3 inhibitor; 20 mg/kg; MedChemExpress, HY-12815) was additionally administered via intraperitoneal injection at 6 h post-transplantation to determine whether the effects of LGALS3 were mediated through the NLRP3 inflammasome pathway. Mice were euthanized at 24 h, 72 h, and seven days after surgery. Liver grafts and peripheral blood samples were rapidly collected. Serum levels of alanine aminotransferase (ALT), aspartate aminotransferase (AST), and total bilirubin (Tbil) were measured using an automated biochemical analyzer (Hitachi 7600, Hitachi Ltd.). Inflammatory cytokines, including IL-1β, IL-18, and TNF-α, were quantified using enzyme-linked immunosorbent assay (ELISA) kits (R&D Systems; M1300, DY912, DY410). Portions of liver tissue were fixed in 4% paraformaldehyde (Electron Microscopy Sciences, 15710) for histopathological and immunohistochemical (IHC) analyses, while the remaining samples were snap-frozen in liquid nitrogen and stored at −80°C for subsequent RNA and protein extraction.

Establishment and treatment of cell models

The human hepatocellular carcinoma cell line HepG2 (ATCC, HB-8065) was purchased from the American Type Culture Collection and routinely cultured in high-glucose DMEM (Gibco, 11965-092) supplemented with 10% fetal bovine serum (Gibco, 10270-106) and 1% penicillin-streptomycin solution (Gibco, 15140-122). Cells were maintained in a humidified incubator at 37 °C with 5% CO_2 (Thermo Scientific, Heracell VIOS 160i). A steatosis model was established by treating cells with a mixture of free fatty acids (FFAs),[33] consisting of oleic acid (Sigma-Aldrich, O1008) and palmitic acid (Sigma-Aldrich, P0500) at a 2:1 ratio. The final working concentration was 500 μM, and cells were incubated for 24 h to induce intracellular lipid accumulation, which was confirmed by Oil Red O staining (Sigma-Aldrich, O0625). For the generation of shLGALS3 and LGALS3 overexpression (OE-LGALS3) cell lines, lentiviral transduction was performed using the pLKO.1 vector (Addgene, #8453). Forty-eight hours post-transduction, cells were subjected to G418 selection (400 μg/mL; Invitrogen, 11811031) for 14 consecutive days. To model I/R stress, cells were first incubated under hypoxic conditions (1% O_2, 5% CO_2, 94% N_2) in a tri-gas incubator (Binder, CB160) for 6 h to simulate the ischemic phase, followed by reoxygenation under normoxic conditions (21% O_2) for 24 h to induce stress-related injury.

Co-immunoprecipitation

Liver tissue samples were lysed in pre-chilled RIPA buffer (Beyotime, P0013B) supplemented with a protease inhibitor cocktail (Roche, 4693132001) and a phosphatase inhibitor mixture (Roche, 4906845001). Homogenates were incubated on a rotator at 4 °C for 30 min, followed by centrifugation at 12,000 × g for 10 min. The supernatants were collected, and protein concentrations were quantified using a BCA Protein Assay Kit (Thermo Fisher Scientific, 23225). Equal amounts of protein (500–800 μg) were incubated overnight at 4 °C with either an anti-LGALS3 antibody (1–2 μg; Abcam, ab2785) or an anti-NLRP3 antibody (1–2 μg; Cell Signaling Technology, #15101) to form immune complexes. Pre-equilibrated Protein A/G magnetic beads (Thermo Fisher Scientific, 88803) were then added and incubated for an additional 2–4 h under gentle rotation to capture the antigen–antibody complexes. After incubation, the beads were washed five times with TBST buffer (Tris-buffered saline containing 0.1% Tween-20; Sigma-Aldrich, P9416) to remove nonspecific binding. A portion of the immunoprecipitated samples was subjected to SDS-PAGE and transferred to membranes for Western blot (WB) analysis. The membranes were probed with anti-NLRP3 and anti-LGALS3 antibodies to verify protein–protein interactions.[34]

WB analysis

Western blotting was performed as previously described.[35] Briefly, total protein was extracted using precooled RIPA lysis buffer supplemented with a protease and phosphatase inhibitor cocktail, and protein concentrations were determined using a BCA Protein Assay Kit. Protein samples (30–50 μg) were separated by 10%–12% SDS–PAGE (Bio-Rad, 456-1096) and subsequently transferred onto 0.22 μm PVDF membranes (Millipore, IPVH00010). Membranes were blocked with 5% non-fat milk for 1 h at ambient temperature and incubated with primary antibodies overnight at 4 °C. After washing the membranes (3 × 5 min), they were incubated with the corresponding HRP-conjugated secondary antibodies (1:5,000, Jackson ImmunoResearch, 111-035-003). Protein bands were visualized using an enhanced chemiluminescence detection reagent (Bio-Rad, 1705060S) and imaged with the ChemiDoc MP Imaging System (Bio-Rad, 12003154). Band intensities were quantified using ImageJ software (v1.53c, NIH) and normalized to the internal control β-actin. All experiments were performed in three independent replicates, and data are presented as mean ± standard deviation. The primary antibodies used were as follows: NLRP3 (1:1,000, Abcam, ab307668), Caspase-1 (1:1,000, Cell Signaling Technology, #2225), IL-1β (1:500, R&D Systems, AF-201-NA), phospho–NF-κB p65 (p–NF-κB) (1:1,000, Cell Signaling Technology, #3033), GSDMD (1:1,000, Abcam, ab209845), ubiquitin (1:2,000, Santa Cruz Biotechnology, sc-8017), Ki67 (1:1,000, Abcam, ab16667), PCNA (1:1,000, Abcam, ab92552), K63-linked ubiquitin (1:1,000, Abcam, ab179434), LGALS3 (1:1,000, Abcam, ab76245), and β-actin (1:5,000, Proteintech, 66009-1-Ig).

Laser confocal imaging

HepG2 cells were washed three times with PBS (pH 7.4) and fixed with 4% paraformaldehyde (Electron Microscopy Sciences, 15710) at ambient temperature for 15 min. Cells were then permeabilized with 0.1% Triton X-100 (Sigma-Aldrich, T9284) for 10 min and blocked with 5% bovine serum albumin (Sigma-Aldrich, A9647) for 1 h to minimize nonspecific binding. Cells were incubated overnight at 4 °C with primary antibodies: anti-LGALS3 (1:200, Abcam, ab2785) and anti-NLRP3 (1:200, Cell Signaling Technology, #15101). After three washes with PBS, Alexa Fluor 488-conjugated goat anti-rabbit IgG (1:500, Invitrogen, A-11008) and Alexa Fluor 594-conjugated goat anti-mouse IgG (1:500, Invitrogen, A-11005) were added and incubated for 1 h in the dark. Nuclei were counterstained with DAPI (1 µg/mL, Invitrogen, D1306) for 5 min, followed by three PBS washes.[36] For mitochondrial mass analysis, cells were incubated with MitoTracker Green FM (200 nM, Invitrogen, M7514) at 37 °C for 30 min and then washed with PBS. For reactive oxygen species (ROS) detection, cells were treated with MitoSOX Red (5 µM, Invitrogen, M36008) at 37 °C for 10 min, followed by PBS washes. All samples were mounted on glass slides using antifade mounting medium (ProLong Gold, Invitrogen, P36930). Fluorescence images were acquired using a laser confocal microscope (Zeiss LSM880, Carl Zeiss, Germany) equipped with a 63× oil immersion objective. Excitation wavelengths were set at 405 nm for DAPI, 488 nm for Alexa Fluor 488, and 561 nm for Alexa Fluor 594 and MitoSOX Red. All images were captured using identical acquisition parameters. Image processing and fluorescence co-localization analyses were performed using ZEN software (Zeiss, v2.6). The Pearson correlation coefficient (R-value) was calculated to evaluate the spatial co-localization between LGALS3 and NLRP3. Signal intensities of MitoTracker and MitoSOX were quantified in ten randomly selected fields. All experiments were independently repeated three times, and mean values were used for statistical analysis.[37]

Histopathological analysis

Liver tissue samples were fixed in 4% paraformaldehyde (Electron Microscopy Sciences, 15710) at 4 °C for 24–48 h, followed by sequential dehydration, clearing, and paraffin embedding. Paraffin blocks were sectioned at 5 µm thickness using a microtome (Leica RM2235), and sections were baked at 65 °C for 1 h. After deparaffinization in xylene and rehydration through graded ethanol, sections were subjected to H&E staining (Sigma-Aldrich, H3401), Masson's trichrome staining (Solarbio, G1340), and Oil Red O staining (Sigma-Aldrich, O0625). All sections were examined and imaged using an Olympus BX53 light microscope (Olympus, Japan). For quantitative analysis, five random high-power fields (400×) were selected per sample. Hepatic inflammation and steatosis were scored according to the modified NAFLD Activity Score (hereinafter referred to as NAS). ImageJ (v1.53c, NIH) and Image-Pro Plus (v6.0, Media Cybernetics) were used to quantify lipid area fractions and fibrotic area percentages. Data represent the mean values of three independent experiments. Histological assessments were performed using a single-blind approach. Two independent investigators, blinded to group allocation and not involved in animal modeling or surgical procedures, evaluated NAS scores and quantified lipid and fibrosis areas. Discrepancies were resolved by consensus, and the averaged values were used for statistical analysis to minimize subjective bias.[38]

IHC and immunofluorescence staining

Paraffin-embedded liver tissue sections (5 µm) were baked at 65 °C for 1 h, deparaffinized in xylene, and rehydrated through a graded ethanol series. Antigen retrieval was performed by microwave heating in citrate buffer (pH 6.0; Beyotime, P0081) for 15 min. After cooling to ambient temperature, sections were incubated with 3% hydrogen peroxide (Solarbio, P0100) for 10 min to block endogenous peroxidase activity, followed by blocking with 5% bovine serum albumin for 1 h to minimize nonspecific binding. Sections were incubated overnight at 4 °C with the following primary antibodies: anti-NLRP3 (1:200, Abcam, ab214185), anti-cleaved caspase-1 (1:100, Cell Signaling Technology, #89332), anti-GSDMD (1:200, Abcam, ab209845), and anti-IL-1β (1:100, R&D Systems, AF-201-NA). After PBS washes, IHC sections were incubated with HRP-conjugated goat anti-rabbit IgG secondary antibody (1:500, Jackson ImmunoResearch, 111-035-003) at ambient temperature for 1 h. Signal development was performed using DAB substrate (ZSGB-BIO, ZLI-9018), followed by hematoxylin counterstaining. Slides were dehydrated, mounted, and imaged using a Nikon Eclipse Ci optical microscope. For immunofluorescence staining, sections were incubated with Alexa Fluor 488- or Alexa Fluor 594-conjugated secondary antibodies (1:500, Invitrogen, A-11008 and A-11005) for 1 h at ambient temperature in the dark, followed by PBS washes. Nuclear staining was performed with DAPI (1 µg/mL, Invitrogen, D1306) for 5 min. Slides were mounted with antifade mounting medium (ProLong Gold, Invitrogen, P36930). Fluorescence images were acquired using a Nikon Eclipse Ti confocal microscope (Nikon, Japan) with excitation wavelengths set at 405 nm for DAPI, 488 nm for Alexa Fluor 488, and 561 nm for Alexa Fluor 594. ImageJ software (v1.53c, NIH) was used to quantify fluorescence intensity in five randomly selected fields. All experiments were repeated at least three times, and mean values were used for statistical analysis.[39]

TUNEL and propidium iodide (PI)/Hoechst double staining

Paraffin-embedded liver sections (5 µm) were deparaffinized in xylene and rehydrated through graded ethanol. Antigen retrieval was performed by microwave heating in citrate buffer (pH 6.0; Beyotime, P0081). After cooling to ambient temperature, sections were permeabilized with 0.1% Triton X-100 (Sigma-Aldrich, T9284) for 10 min. DNA fragmentation was detected using the In Situ Cell Death Detection Kit (Roche, 11684817910), and the TUNEL reaction was carried out according to the manufacturer's instructions.[40] Sections were incubated for 1 h at ambient temperature in the dark, washed with PBS, and counterstained with DAPI (1 µg/mL, Invitrogen, D1306) for 5 min. Combined detection of pyroptosis and apoptosis was performed using PI/Hoechst double staining.[41] Sections were incubated with a staining solution containing PI (5 µg/mL, Sigma-Aldrich, P4170) and Hoechst 33342 (10 µg/mL, Invitrogen, H3570) at 37 °C for 15 min in the dark. Following PBS washes, sections were mounted with antifade mounting medium (ProLong Gold, Invitrogen, P36930). Fluorescence images were acquired using an Olympus IX73 fluorescence microscope (Olympus, Japan), with excitation wavelengths set at 405 nm (DAPI), 535 nm (PI), and 350 nm (Hoechst). TUNEL-positive cells exhibited green fluorescence, PI-positive cells displayed red fluorescence, and Hoechst-positive nuclei appeared blue. Five random high-power fields (400×) were selected per section to calculate the proportion of TUNEL- and PI-positive cells. Quantitative image analysis was performed using ImageJ software (v1.53c, NIH). All experiments were conducted in three independent replicates, and mean values were used for subsequent statistical analyses.

Liver function assessment and inflammatory cytokine measurement

At designated time points post-surgery, mouse blood was collected via retro-orbital venipuncture and transferred into non-anticoagulant centrifuge tubes. Serum was separated by centrifugation at 3,000 × g for 10 min at 4 °C and then immediately stored at −80°C for subsequent analysis. Liver function tests were performed after the samples were thawed to ambient temperature. Serum levels of ALT, AST, and Tbil were measured using an automated biochemical analyzer (Hitachi 7600, Hitachi High-Technologies, Japan).[42] Inflammatory cytokines, including mouse IL-1β (R&D Systems, M1300), IL-18 (R&D Systems, DY912), and TNF-α (R&D Systems, DY410), were quantified using ELISA kits. Standard curves were prepared according to the instructions, and both samples and standards were incubated in 96-well plates under light-protected conditions at ambient temperature. After adding the stop solution, absorbance was measured at 450 nm using a microplate reader (BioTek Epoch 2, Agilent Technologies, USA) for quantitative analysis. All measurements were performed in duplicate, with a minimum of six samples per group, and each experiment was repeated three times to ensure data reliability.[43]

Prediction of NLRP3 ubiquitination sites

The protein sequence of human NLRP3 (NCBI Reference Sequence: NP_004886.3) was retrieved from the NCBI database (https://www.ncbi.nlm.nih.gov/). Using this FASTA sequence as input, ubiquitination site prediction was performed with the MusiteDeep online tool (https://www.musite.net/), applying a score threshold of 0.5 to identify putative modification sites. Predicted ubiquitination sites with scores ≥ 0.5 were considered potential PTM sites, in accordance with previous computational proteomics approaches.[44]

RNA-seq and data analysis

In a semi-orthotopic liver transplantation model established using steatotic livers induced by an HFD, graft tissues were collected 24 h post-transplantation from the Fat + Tx group (n = 3), along with normal liver tissues from the Sham group (n = 3), for RNA-seq analysis. Total RNA was extracted from mouse liver tissues using TRIzol reagent (T9424, Sigma, USA). RNA purity was assessed by measuring the OD260/280 ratio using a NanoDrop 2000 spectrophotometer (Thermo Fisher Scientific, USA), and RNA integrity was evaluated with an Agilent 2100 Bioanalyzer (Agilent Technologies, USA), with samples showing an RNA Integrity Number ≥ 7.0 considered acceptable. Library construction was performed using the TruSeq Stranded mRNA Library Prep Kit (20020594, Illumina, USA). mRNA was enriched by poly-A selection, fragmented, reverse-transcribed into cDNA, end-repaired, and adapter-ligated. The final libraries were sequenced on an Illumina NovaSeq 6000 platform to generate 150 bp paired-end reads.

Raw sequencing data were subjected to quality control using FastQC (v0.11.9) to remove low-quality reads and adapter contamination. Clean reads were aligned to the mouse reference genome (GRCm38/mm10) using HISAT2 (v2.1.0), with alignment rates > 95% considered satisfactory. Gene-level read counts were obtained using featureCounts (Subread v2.0.1), and transcript abundance was normalized as fragments per kilobase of transcript per million mapped reads. Differential expression analysis was performed using the limma package (v3.64.3) in R. Genes with $|\log_2 \text{fold change}| > 1$ and adjusted *P*-value (adj.P.Val) < 0.05 were defined as differentially expressed genes (DEGs). This threshold is widely used in transcriptomic studies as a high-confidence criterion, ensuring biologically meaningful expression changes of at least twofold while controlling the false discovery rate using the Benjamini–Hochberg method, which is particularly suitable for small-sample animal experiments (n = 3 per group). DEG results were visualized using volcano plots and heatmaps generated with the pheatmap package (v1.0.12). Functional annotation and pathway enrichment analyses were conducted using the clusterProfiler package (v4.4.0), based on the Gene Ontology (GO) and Kyoto Encyclopedia of Genes and Genomes (KEGG) databases. Significantly enriched pathways were visualized as bubble plots. To identify key regulatory genes, DEGs were further subjected to least absolute shrinkage and selection operator (LASSO) regression using the glmnet package (v4.1-10) and to support vector machine recursive feature elimination analysis using the caret package (v7.0-1). Venn diagram analysis was performed using the VennDiagram package (v1.7.3) to identify overlapping candidate genes.[45,46]

Statistical analysis

All data were derived from at least three independent experiments and are presented as mean ± standard deviation. Comparisons between two groups were conducted using an independent-samples t-test. For comparisons involving three or more groups, one-way analysis of variance was employed. If analysis of variance indicated significant differences, Tukey's HSD test was subsequently applied for pairwise group comparisons. For datasets that did not meet the assumptions of normality or homogeneity of variance, nonparametric tests, including the Mann–Whitney U test and the Kruskal–Wallis H test, were used as appropriate. Postoperative survival was analyzed using the Kaplan–Meier method, with death defined as the event of interest and postoperative observation time (0–14 days) as the time variable. Mice that survived until the end of the observation period were treated as censored cases. Survival curves among the five groups (Sham, Fat + Tx, Fat + Tx + siLGALS3, Fat + Tx + ML265, and Fat + Tx + ML265 + MCC950) were compared using the log-rank (Mantel–Cox) test to evaluate the effects of different interventions on 14-day postoperative survival. All statistical analyses were performed using GraphPad Prism 9.5.0 (GraphPad Software, Inc.) and R version 4.2.1 (R Foundation for Statistical Computing). A two-tailed *P*-value < 0.05 was considered statistically significant.

Results

LGALS3 may play a critical role in postoperative injury of steatotic liver grafts by regulating inflammasome activation

A semi-orthotopic liver transplantation model was established in mice with hepatic steatosis induced by an HFD. At 24 h post-transplantation, graft tissues from the Fat + Tx group (n = 3) and normal liver tissues from the Sham group (n = 3) were collected for RNA-seq analysis (Fig. 1A). Differential expression analysis revealed 143 DEGs between the Fat + Tx and Sham groups ($|\log_2 FC| > 1$, adjusted *P*-value < 0.05), with 121 genes upregulated and 22 genes downregulated (Fig. 1B). The expression patterns of the 22 downregulated genes and the top 40 upregulated genes are shown in Figure 1C. In addition, we compared the DEGs identified in this study with those reported in previous transcriptomic studies of steatotic liver injury and I/R. Consistent with earlier reports, genes involved in inflammasome activation and pyroptosis, such as *Nlrp3, Il1b, Casp1, Gsdmd, Ccl2, S100a8, S100a9*, and *Tnf*, were consistently and significantly upregulated in NAFLD/NASH and steatotic transplantation models.[47–50] These expression patterns closely mirrored those observed in the Fat + Tx group in the present study.

To further characterize the biological significance of the upregulated DEGs, GO and KEGG enrichment analyses were performed. GO analysis revealed significant enrichment in biological processes related to pyroptosis, inflammasome complex assembly, and cytokine receptor binding, suggesting enhanced activation of pyroptotic signaling following steatotic liver transplantation (Fig. 1D). KEGG pathway analysis further revealed significant activation of the NOD-like receptor signaling pathway, alcoholic liver disease pathway, and NF-κB signaling pathway in the Fat + Tx group (Fig. 1E). Furthermore, accumulating transcriptomic evidence from steatotic grafts and I/R-related hepatic injury models consistently indicates enrichment of inflammatory pathways, including NF-κB, NOD-like receptor, and IL-1β/IL-18-associated signaling cascades. These pathways showed a high degree of concordance with those identified in the present study.[51–54] This cross-study consistency supports the robustness of our transcriptomic analysis and suggests that steatotic liver grafts undergo a canonical, pyroptosis-dominated inflammatory injury process during the early post-transplant period, centered on the NLRP3-caspase-1-GSDMD axis.

To identify key genes mediating postoperative injury in steatotic liver grafts, two machine learning algorithms were employed. The LASSO algorithm identified six candidate genes (Fig. 1F), while the support vector machine recursive feature elimination algorithm yielded 40 candidates (Fig. 1G). Intersection of these two gene sets revealed *Lgals3* as the most prominent overlapping candidate (Fig. 1H), with significantly higher expression in the Fat + Tx group compared to the Sham group (Fig. 1I). Furthermore, WB analysis of clinical liver samples was performed to examine the expression of LGALS3 and NLRP3 in different donor livers before and after perfusion. The results confirmed that both LGALS3 and NLRP3 were markedly upregulated in steatotic donor livers (Fig. 1J). These findings suggest that LGALS3 may play a pivotal role in postoperative injury of steatotic liver grafts by modulating inflammasome activation.

LGALS3 promotes activation of the NLRP3-IL-1β-NF-κB signaling axis and pyroptosis in the HepG2-FFA I/R model

shLGALS3 and OE-LGALS3 cell lines were established in a human steatotic hepatocyte model (HepG2 cells induced with FFA). Under I/R stress, pyroptosis levels and the expression of key signaling molecules were assessed (Fig. 2A). Lactate dehydrogenase release assays indicated that I/R stress induced substantial cell damage. Compared with the control group, lactate dehydrogenase release decreased in the sh-LGALS3 group (*P* = 0.003) but markedly increased in the OE-LGALS3 group (*P* = 0.001) (Fig. 2B). Consistently, WB analysis demonstrated that protein levels of NLRP3, cleaved caspase-1, IL-1β, and phosphorylated NF-κB p65 were significantly elevated in the OE-LGALS3 group, whereas these pyroptosis-related proteins were markedly downregulated in the shLGALS3 group (*P* < 0.01, Fig. 2C).

To further investigate NLRP3 inflammasome assembly and its colocalization with LGALS3, laser confocal microscopy was performed. Strong colocalization between NLRP3 and LGALS3 was observed in the OE-LGALS3 group (Pearson's R = 0.81, *P* < 0.001), whereas this interaction was markedly attenuated in the shLGALS3 group (Fig. 2D). MitoTracker and MitoSOX assays demonstrated a significant decrease in mitochondrial membrane potential and an increase in ROS production in the OE-LGALS3 group, while the shLGALS3 group maintained mitochondrial homeostasis with reduced ROS levels (Fig. 2E and F).

These findings suggest that LGALS3 promotes activation of the NLRP3-IL-1β-NF-κB signaling axis and enhances pyroptosis in the HepG2-FFA I/R model.

LGALS3 promotes NLRP3 activation by suppressing site-specific ubiquitination

To systematically investigate the molecular mechanism by which LGALS3 regulates the ubiquitination of NLRP3, an HA-ubiquitin expression plasmid was constructed. Under treatment with the proteasome inhibitor MG132, the level of NLRP3 ubiquitination was assessed using co-immunoprecipitation assays. In the OE-LGALS3 group, ubiquitination of NLRP3 was reduced (*P* = 0.008), suggesting that OE-LGALS3 suppresses NLRP3 ubiquitination. Conversely, in the shLGALS3 group, NLRP3 ubiquitination was enhanced (*P* = 0.001) (Fig. 3A and B). Following K63-linked ubiquitin overexpression, we demonstrated that the K63 ubiquitination level of NLRP3 was significantly reduced in the OE-LGALS3 group, whereas it was markedly increased in the shLGALS3 group (Fig. 3A and B).

To identify potential ubiquitination sites, MusiteDeep was used to predict PTMs on NLRP3, with sites scoring above 0.5 shown in Figure 3C. Based on these results, lysine 192 (K192), which exhibited the highest PTM score, was selected for site-directed mutagenesis to generate a ubiquitination-deficient NLRP3 $K \rightarrow R$ mutant (Fig. 3D). This mutant was used to assess the functional relevance of site-specific ubiquitination. In the OE-LGALS3 group, the $K \rightarrow R$ mutant of NLRP3 failed to induce the upregulation of pyroptosis-associated proteins such as IL-1β, Caspase-1, and GSDMD-N. Compared with the wild type, IL-1β expression in the mutant condition was significantly reduced (*P* < 0.01), with markedly lower levels of Caspase-1 and GSDMD-N as well (Fig. 3E).

Taken together, these results indicate that LGALS3 negatively regulates NLRP3 activation and its downstream pyroptosis signaling axis by modulating site-specific ubiquitination of NLRP3.

Functional evaluation of LGALS3 intervention in an orthotopic steatotic liver transplantation model

In a BALB/c mouse orthotopic liver transplantation model, an HFD was used to successfully induce steatotic donor livers (Fig. 4A). Specifically, mice were divided into five groups: Sham, Fat + Tx, Fat + Tx + siLGALS3, Fat + Tx + ML265, and Fat + Tx + ML265 + MCC950 (n = 15 per group) to comprehensively evaluate the role of LGALS3 intervention in post-transplant liver function recovery and inflammatory re-

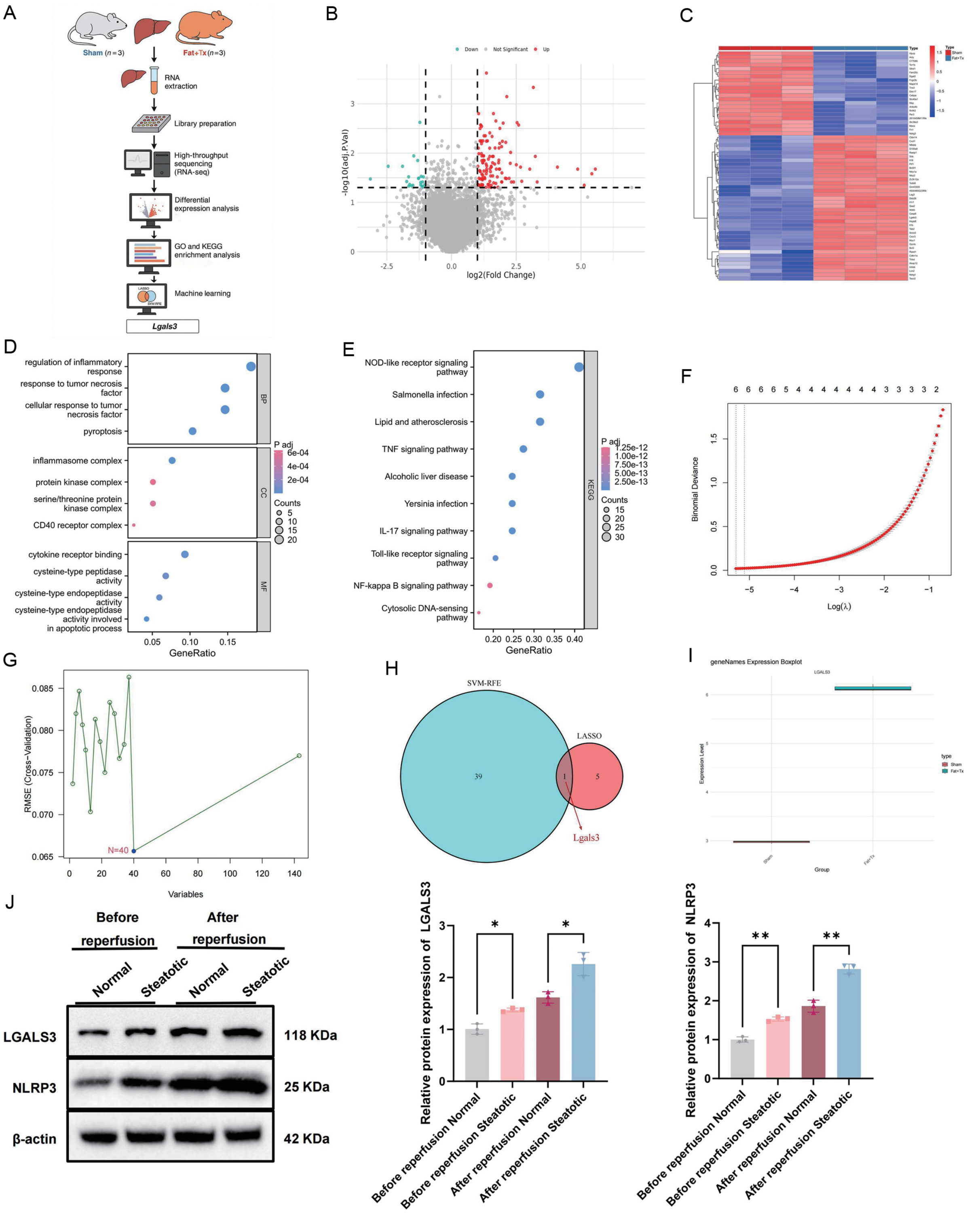

Fig. 1. RNA-seq landscape of pyroptosis following steatotic liver graft transplantation. (A) Schematic illustration of the experimental workflow for the semi-orthotopic liver transplantation mouse model. (B) Volcano plot of DEGs between the Fat + Tx and Sham groups identified by RNA sequencing (red: upregulated; green: downregulated; gray: not significant). (C) Heatmap displaying 22 downregulated and the top 40 upregulated DEGs (n = 3). (D) GO functional enrichment analysis. (E) KEGG pathway enrichment analysis. (F) Key gene selection using the LASSO algorithm. (G) Key gene selection using the SVM-RFE algorithm. (H) Overlapping key genes identified by both LASSO and SVM-RFE algorithms. (I) RNA-seq data showing the expression level of Lgals3 in the Fat + Tx group. (J) Western blot analysis of LGALS3 and NLRP3 expression in hepatocytes from donor livers before and after perfusion. Normal liver donors (n = 45); steatotic liver donors (n = 45). $*P < 0.05$, $**P < 0.01$. DEGs, differentially expressed genes; RNA, ribonucleic acid; GO, Gene Ontology; KEGG, Kyoto Encyclopedia of Genes and Genomes; LASSO, least absolute shrinkage and selection operator; SVM-RFE, support vector machine–recursive feature elimination; LGALS3, galectin-3; RNA-seq, RNA sequencing.

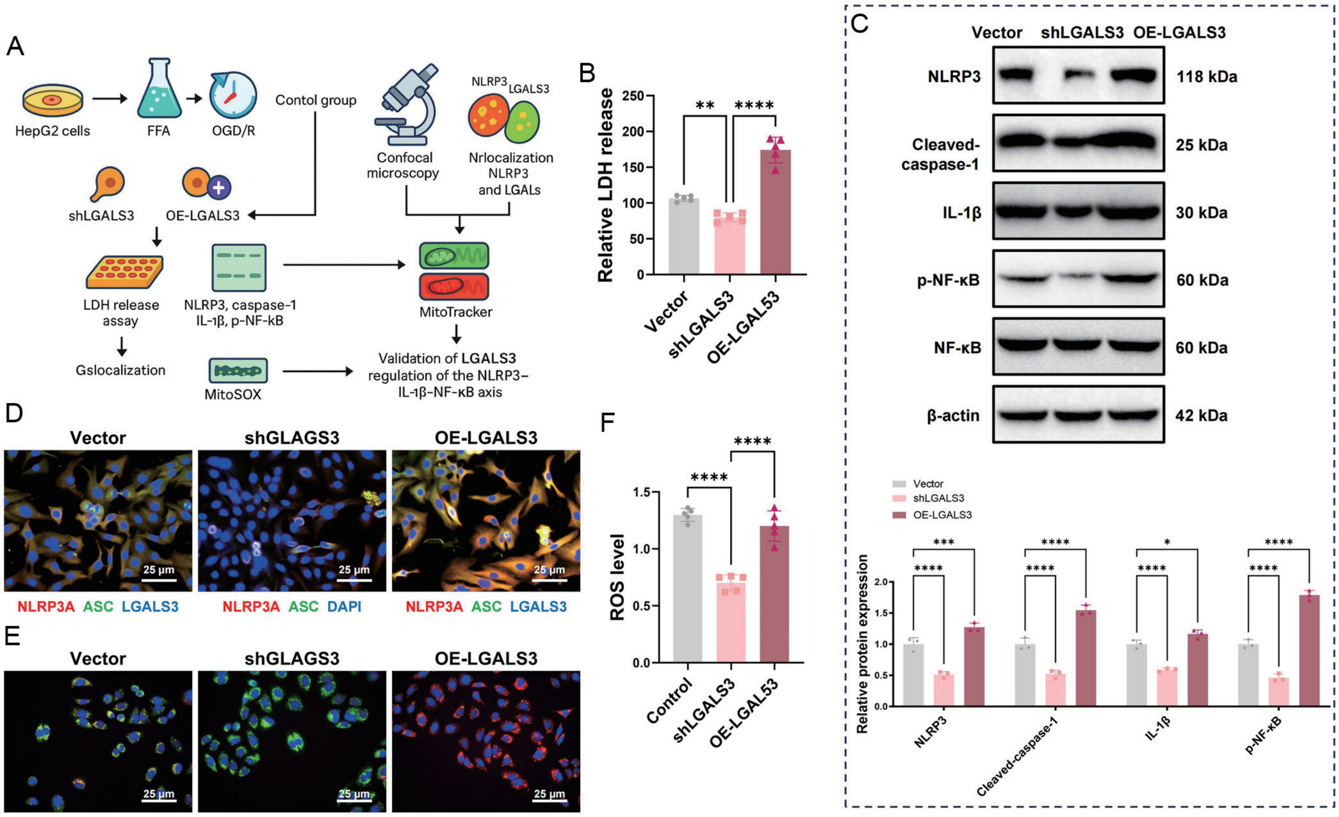

Fig. 2. ***In vitro* functional validation of LGALS3 regulation of the NLRP3-IL1β-NF-κB axis.** (A) Schematic diagram of the *in vitro* experimental workflow assessing the regulatory effect of LGALS3 on the NLRP3-IL-1β-NF-κB axis. (B) Assessment of cellular pyroptosis levels by measuring lactate dehydrogenase (LDH) release in each group. (C) Western blot analysis showing the expression levels of key proteins: NLRP3, cleaved caspase-1, IL-1β, and p-NF-κB, with β-actin as the internal control. (D) Confocal laser scanning microscopy showing the subcellular localization and colocalization of NLRP3 and LGALS3 (green: NLRP3; red: LGALS3; yellow: colocalized regions). (E–F) MitoTracker (E) and MitoSOX (F) assays assessing mitochondrial homeostasis and ROS production; ROS levels are markedly elevated in the OE-LGALS3 group and reduced in the shLGALS3 group. Data are presented as mean ± SD (n = 3). **P* < 0.05, ***P* < 0.01, ****P* < 0.001, *****P* < 0.0001. siLGALS3, small interfering RNA targeting galectin-3; OE-LGALS3, galectin-3 overexpression vector; NLRP3, NOD-like receptor pyrin domain-containing protein 3; IL-1β, interleukin-1 beta; NF-κB, nuclear factor kappa-light-chain-enhancer of activated B cells; ASC, apoptosis-associated speck-like protein containing a CARD; DAPI, 4′,6-diamidino-2-phenylindole; LDH, lactate dehydrogenase; ROS, reactive oxygen species; SD, standard deviation.

sponse. Serum biochemical analysis revealed significantly elevated levels of ALT (350 ± 28 U/L), AST (420 ± 35 U/L), and Tbil (3.2 ± 0.3 mg/dL) in the Fat + Tx group compared with the Sham group ($P < 0.001$) (Fig. 4B–D). siLGALS3 group led to a marked reduction in ALT to 190 ± 15 U/L ($P < 0.001$ vs. Fat + Tx), a decrease in AST ($P < 0.001$), and a significant improvement in Tbil levels. The ML265 group exhibited a similar trend to that observed in the siLGALS3 group.

ELISA was performed to quantify the levels of IL-1β and IL-18 in each group. The results showed that, compared with the Sham group, both cytokines were significantly elevated in the Fat + Tx group ($P < 0.001$). In contrast, siLGALS3 knockdown or ML265 treatment markedly reduced the levels of these inflammatory mediators ($P < 0.01$). In the rescue experiment, the ML265 + MCC950 group exhibited a further reduction in IL-1β and IL-18 levels ($P < 0.01$), indicating that inhibition of NLRP3 inflammasome activity synergistically enhanced the anti-inflammatory effects mediated by LGALS3 targeting (Fig. 4E and F).

ROS measurements revealed that hepatic ROS levels in the Fat + Tx group were elevated compared to the Sham group ($P < 0.001$), while siLGALS3 treatment significantly reduced ROS levels to near-normal ($P = 0.002$) (Fig. 4G and H). IHC analysis showed marked upregulation of LGALS3 expression in the Fat + Tx group, which was effectively suppressed by both siLGALS3 and ML265 treatment (Fig. 4I). WB analysis of LGALS3 expression across the different groups was consistent with the IHC findings (Fig. 4J).

Inhibition of LGALS3 and the NLRP3 signaling pathway significantly attenuates hepatocyte pyroptosis and tissue injury following steatotic liver graft transplantation

H&E staining revealed that hepatocytes in the Sham group maintained intact cellular architecture without evident pathological alterations. In contrast, the Fat + Tx group showed pronounced hepatocellular ballooning degeneration accompanied by extensive inflammatory cell infiltration, resulting in a significantly elevated inflammation score. Following siLGALS3 intervention, the inflammatory response was markedly attenuated compared with the Fat + Tx group, as evidenced by a significant reduction in the inflammation score ($P < 0.001$). Similar improvements were observed in the ML265-treated group ($P < 0.001$). Notably, combined treatment with the NLRP3 inhibitor MCC950 further reduced the inflammation score ($P < 0.001$) (Fig. 5A–C).

Masson's trichrome staining demonstrated a significant increase in collagen deposition in the Fat + Tx group relative to the Sham group ($P < 0.001$). Treatment with siLGALS3 and

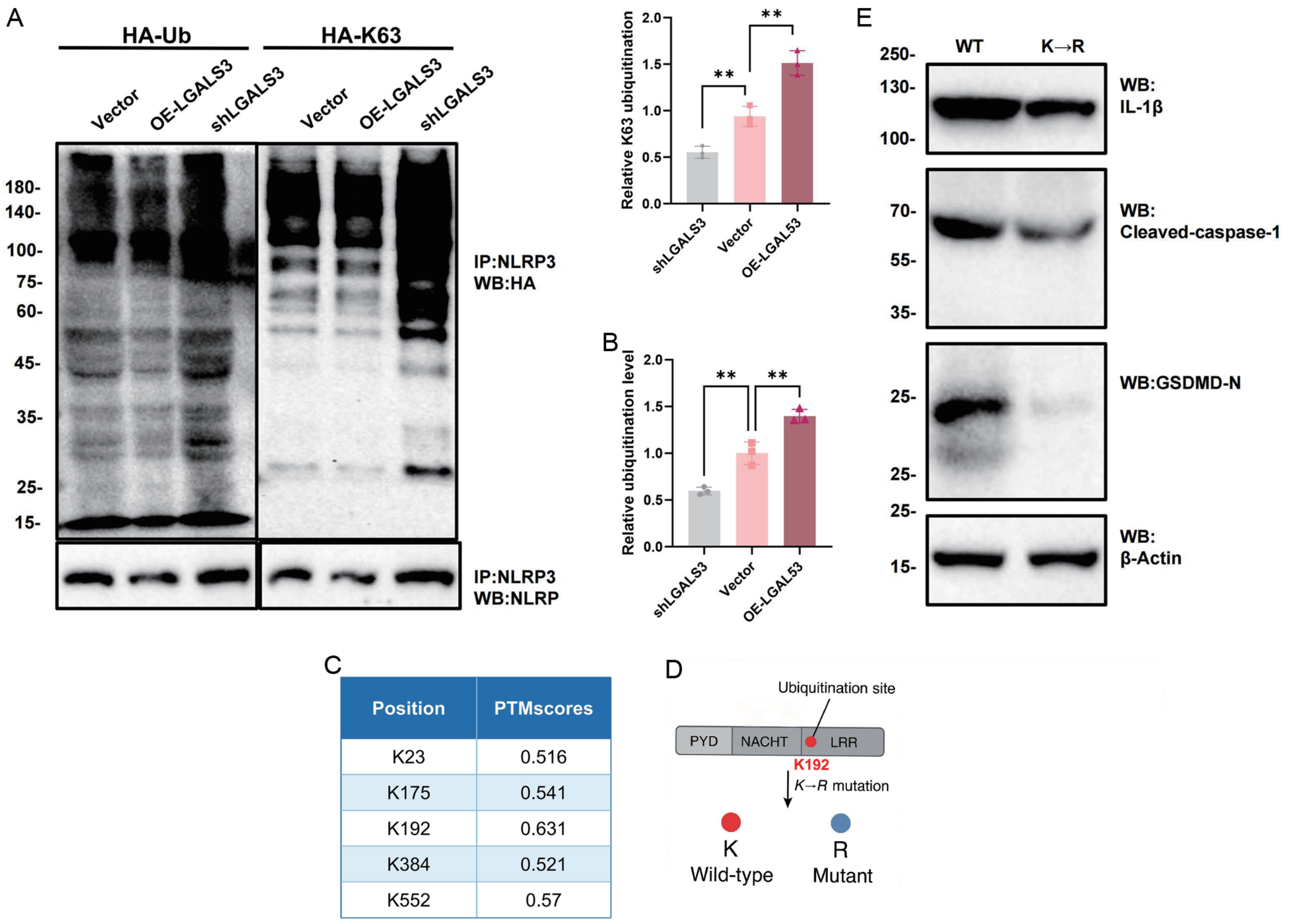

Position	PTMscores
K23	0.516
K175	0.541
K192	0.631
K384	0.521
K552	0.57

Fig. 3. Effects of LGALS3 on NLRP3 ubiquitination and the pyroptosis signaling axis. (A) Immunoprecipitation analysis showing ubiquitination signals of NLRP3 in different experimental groups. (B) Quantitative analysis of total ubiquitination and K63-linked ubiquitination (K63-Ub) levels of NLRP3. (C) Prediction of potential ubiquitination sites on NLRP3 using the MusiteDeep database. (D) Schematic representation of site-directed K→R (lysine-to-arginine) mutations in predicted NLRP3 ubiquitination sites. (E) Western blot analysis of IL-1β, caspase-1, and GSDMD-N expression in cells expressing wild-type NLRP3 or K→R mutant constructs under OE-LGALS3 conditions. Data are presented as mean ± SD (n = 3). $^{**}P < 0.01$. K→R, lysine-to-arginine mutation; WT, wild-type; WB, Western blot; GSDMD-N, gasdermin D N-terminal domain; IP, immunoprecipitation; HA, hemagglutinin tag; PTM, post-translational modification; PYD, pyrin domain; K63-Ub, K63-linked ubiquitin; OE-LGALS3, LGALS3 overexpression.

ML265 reduced the fibrosis area ($P < 0.01$), while the ML265 + MCC950 combination showed the most substantial reduction ($P < 0.001$) (Fig. 5D and E).

Oil Red O staining demonstrated a marked increase in intracellular lipid droplet accumulation in the Fat + Tx group ($P < 0.001$). Both siLGALS3 and ML265 interventions significantly decreased lipid burden, with the ML265 + MCC950 group exhibiting the greatest improvement (Fig. 5F).

IHC revealed significantly elevated expression of NLRP3, cleaved caspase-1, GSDMD, and IL-1β proteins in the Fat + Tx group compared to the Sham group ($P < 0.001$). All therapeutic interventions, including siLGALS3, ML265, and ML265 + MCC950, significantly suppressed the expression of these pyroptosis-associated proteins ($P < 0.001$) (Fig. 6A and B). WB analysis confirmed the findings from IHC (Fig. 6C).

TUNEL staining and PI/Hoechst dual staining further demonstrated a significant increase in pyroptosis-positive cells in the Fat + Tx group, whereas siLGALS3 knockdown or ML265 treatment markedly reduced the percentage of pyroptotic cells ($P < 0.001$). Notably, the ML265 + MCC950 group exhibited the lowest proportion of pyroptosis-positive cells ($P < 0.001$) (Fig. 6D–G). These findings indicate that inhibition of LGALS3 and the NLRP3 signaling pathway markedly attenuates hepatocyte pyroptosis and tissue injury following steatotic liver graft transplantation.

Systematic evaluation of liver function recovery and survival prognosis

To systematically evaluate the effects of each intervention on graft regeneration and postoperative prognosis (Fig. 7A), we first assessed the expression of hepatocyte proliferation markers Ki67 and PCNA (Fig. 7B and E). In the Fat + Tx group, the proportion of Ki67-positive cells in liver tissue was significantly reduced relative to the Sham group, indicating impaired regenerative capacity. In contrast, siLGALS3 and ML265 treatments markedly increased the Ki67-positive rates ($P < 0.001$), while the combination of ML265 with MCC950 partially attenuated this improvement ($P < 0.01$ vs. ML265 group). The IHC findings for PCNA were consistent with those for Ki67 (Fig. 7C and F). WB analysis further confirmed that the expression levels of Ki67 and PCNA exhibited trends consistent with the IHC findings (Fig. 7D and G).

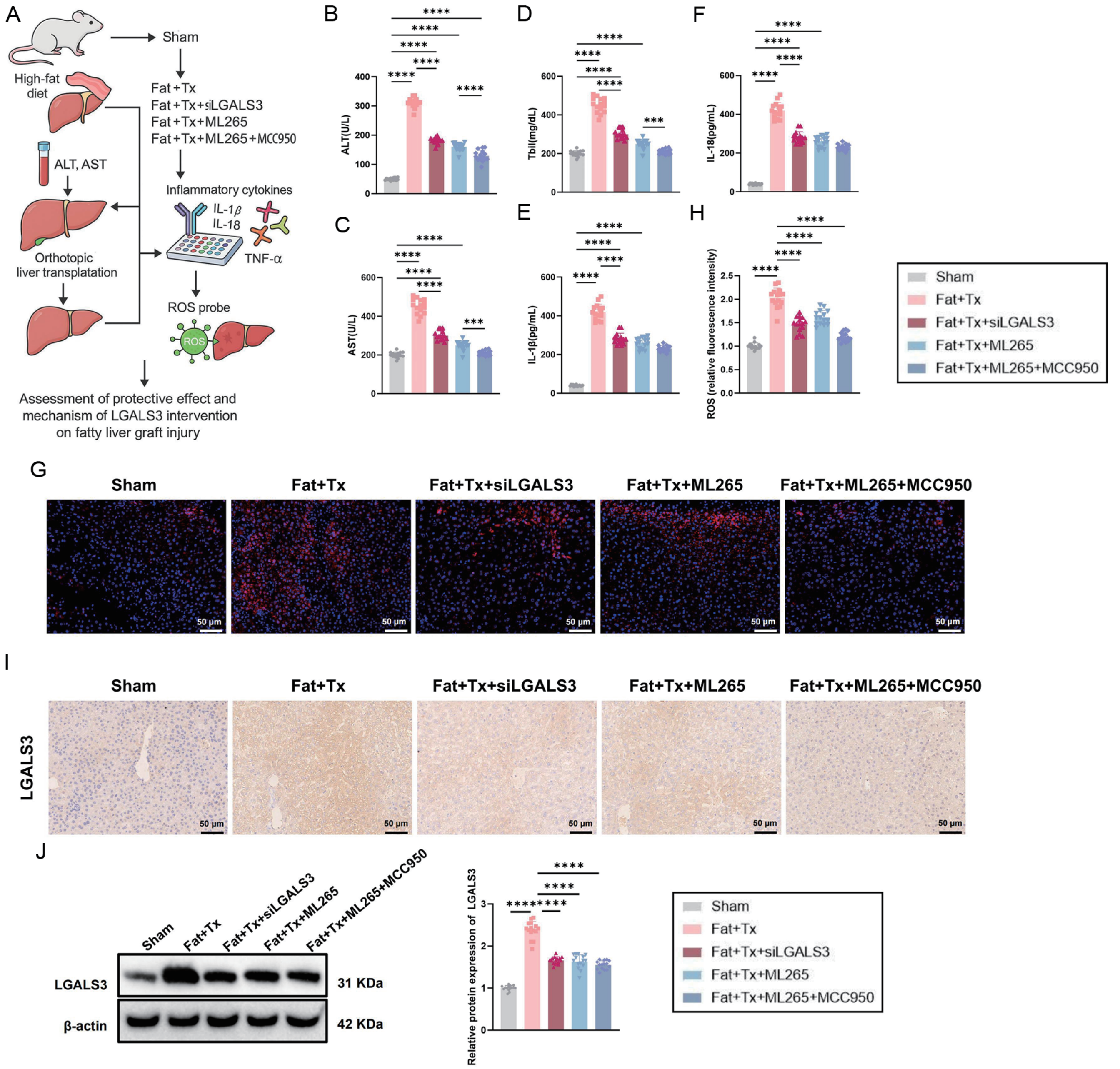

Fig. 4. Effects of LGALS3 intervention in a steatotic liver transplantation model. (A) Schematic illustration of the experimental design for the orthotopic liver transplantation mouse model. (B–D) Serum levels of alanine aminotransferase (ALT), aspartate aminotransferase (AST), and total bilirubin (Tbil) measured on postoperative day 3 in each group. (E–F) Serum concentrations of interleukin-1β (IL-1β) and interleukin-18 (IL-18) determined by ELISA. (G) Detection of reactive oxygen species (ROS) levels in transplanted liver tissues using a fluorescent probe. (H) Quantification of relative ROS fluorescence intensity. (I) Immunohistochemical staining of LGALS3 expression in mouse liver tissues (original magnification, 200×). (J) Western blot analysis of LGALS3 expression in liver grafts. Data are presented as mean ± SD (n = 15). ****$P < 0.0001$.ALT, alanine aminotransferase; AST, aspartate aminotransferase; Tbil, total bilirubin; IL-1β, interleukin-1 beta; IL-18, interleukin-18; ROS, reactive oxygen species; ELISA, enzyme-linked immunosorbent assay; SD, standard deviation; LGALS3, galectin-3.

Doppler ultrasound analysis showed that hepatic hemodynamic parameters, including portal vein flow velocity and hepatic artery resistance index, were significantly decreased in the Fat + Tx group relative to the Sham group, whereas both siLGALS3 and ML265 interventions improved hepatic blood flow dynamics (Fig. 7H and I). The ML265 + MCC950 group exhibited a less pronounced improvement compared to the ML265 group alone ($P < 0.05$). Postoperative survival analysis revealed that the 7-day and 14-day survival rates in the Fat + Tx group were 40% and 25%, respectively, relative to the Sham group. In contrast, siLGALS3 knockdown or ML265 treatment significantly improved postoperative survival compared with the Fat + Tx group ($P < 0.001$). Notably, the group receiving combined ML265 and MCC950 treatment showed a lower survival rate than the ML265 group (Fig. 7J).

To further assess neurological outcomes associated with

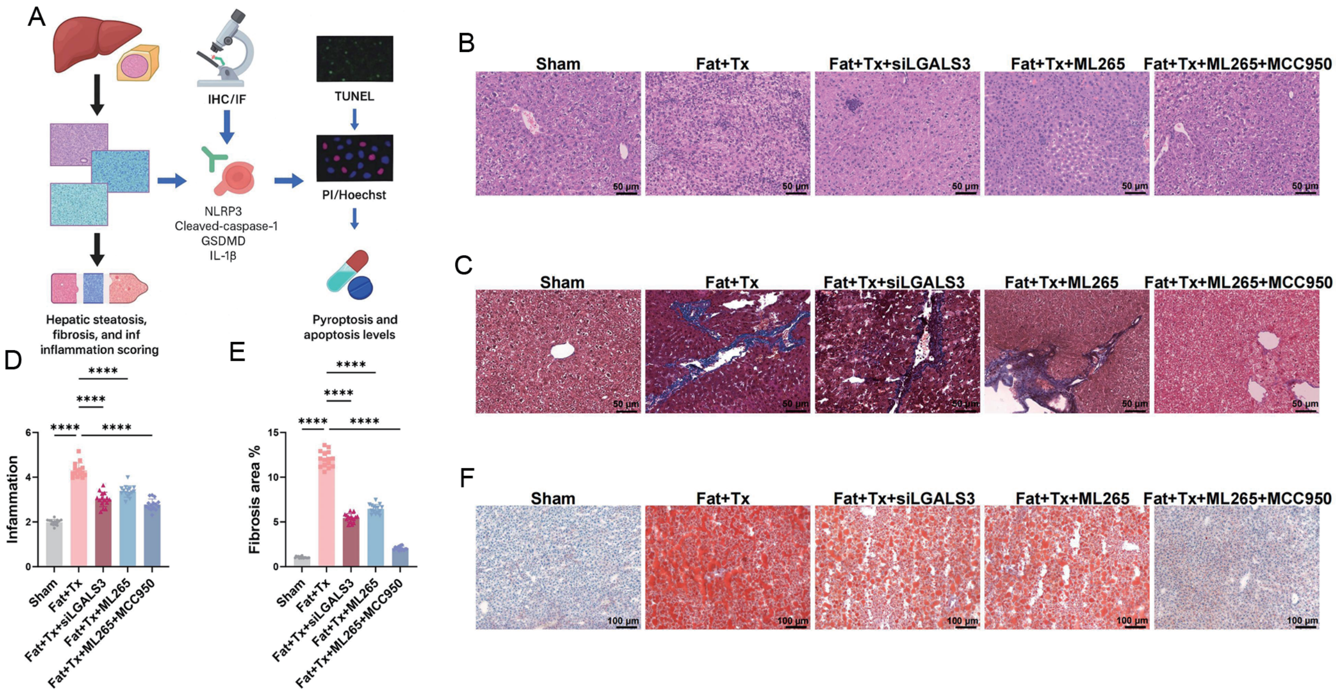

Fig. 5. Histopathological and lipid deposition analyses of liver grafts following LGALS3 and NLRP3 pathway modulation. (A) Schematic overview of the experimental workflow for histopathological analyses. (B) Representative hematoxylin and eosin (H&E) staining of liver grafts in each group. (C) Quantitative analysis of hepatic inflammation scores based on the modified NAFLD activity score (NAS). (D) Masson's trichrome staining of liver tissues. (E) Quantification of fibrotic area in liver grafts. (F) Oil Red O staining showing lipid accumulation in liver tissues. Data are presented as mean ± SD (n = 15). ****$P < 0.0001$. H&E, hematoxylin and eosin; NAS, NAFLD activity score; NAFLD, nonalcoholic fatty liver disease; SD, standard deviation; LGALS3, galectin-3; NLRP3, NOD-like receptor pyrin domain-containing protein 3.

encephalopathic inflammation, cognitive function was evaluated using the Y-maze test. The Fat + Tx group exhibited a significant reduction in spontaneous alternation rate compared with the Sham group ($P < 0.01$), suggesting cognitive impairment. siLGALS3 intervention or ML265 treatment significantly improved this deficit ($P < 0.01$ vs. Fat + Tx group), whereas the ML265 + MCC950 group showed only limited improvement (Fig. 7K).

Discussion

This study systematically elucidated the molecular mechanisms underlying pyroptosis activation following steatotic liver graft transplantation and identified LGALS3 as a key regulator of the NLRP3 inflammasome and its ubiquitination. These findings not only deepen the current understanding of the pathogenesis of post-transplant complications associated with steatotic grafts but also highlight LGALS3 as a promising therapeutic target for improving clinical outcomes in recipients of steatotic donor livers. Notably, the proportion of steatotic donor livers used in clinical transplantation has steadily increased and now constitutes a major limiting factor for transplant success.[55,56] Although previous studies have linked the vulnerability of steatotic donor livers to microcirculatory dysfunction, oxidative stress, and metabolic disturbances, the contribution of programmed cell death, particularly pyroptosis, to post-transplant graft injury remains underexplored.[57–59] By performing transcriptomic profiling, we observed marked upregulation of inflammation- and pyroptosis-related genes in steatotic grafts at 24 h post-transplantation, indicating that pyroptosis may serve as a central driver of early graft injury.

Historically, research on post-transplant graft dysfunction has focused predominantly on apoptosis and necrosis. However, pyroptosis, a form of programmed cell death dependent on inflammasome activation, has received little attention in the context of steatotic liver grafts .[60,61] Our RNA-seq analysis revealed significant enrichment of pyroptosis-related genes, as well as components of the NOD-like receptor and NF-κB signaling pathways. By integrating machine learning algorithms, LGALS3 was identified as a potential key regulatory factor. These findings suggest that LGALS3 may influence graft injury by modulating inflammasome assembly and activation, consistent with its previously reported roles in hepatic fibrosis and regulation of the tumor microenvironment.[26,62] Notably, this study is the first to implicate LGALS3 in the regulation of pyroptosis following steatotic liver graft transplantation. Current strategies aimed at improving outcomes after steatotic liver transplantation have predominantly focused on donor management, including enhanced donor assessment to avoid severe hepatic steatosis[63] and the development of advanced organ preservation technologies for steatotic grafts.[55] However, in the present study, we primarily propose novel therapeutic strategies targeting the recipient, which may be more forward-looking, given that donor liver steatosis is now widely reported and increasingly unavoidable in clinical liver transplantation.[64] Previous studies have demonstrated that berberine can protect transplanted steatotic livers by inhibiting endoplasmic reticulum stress,[65] and that liver regeneration-enhancing agents can alleviate I/R injury in fatty livers.[66] Consistent with and extending these findings, our results provide a novel therapeutic perspective for mitigating complications associated with steatotic liver transplantation, highlighting the potential value of recipient-oriented interventions in improving post-transplant outcomes.

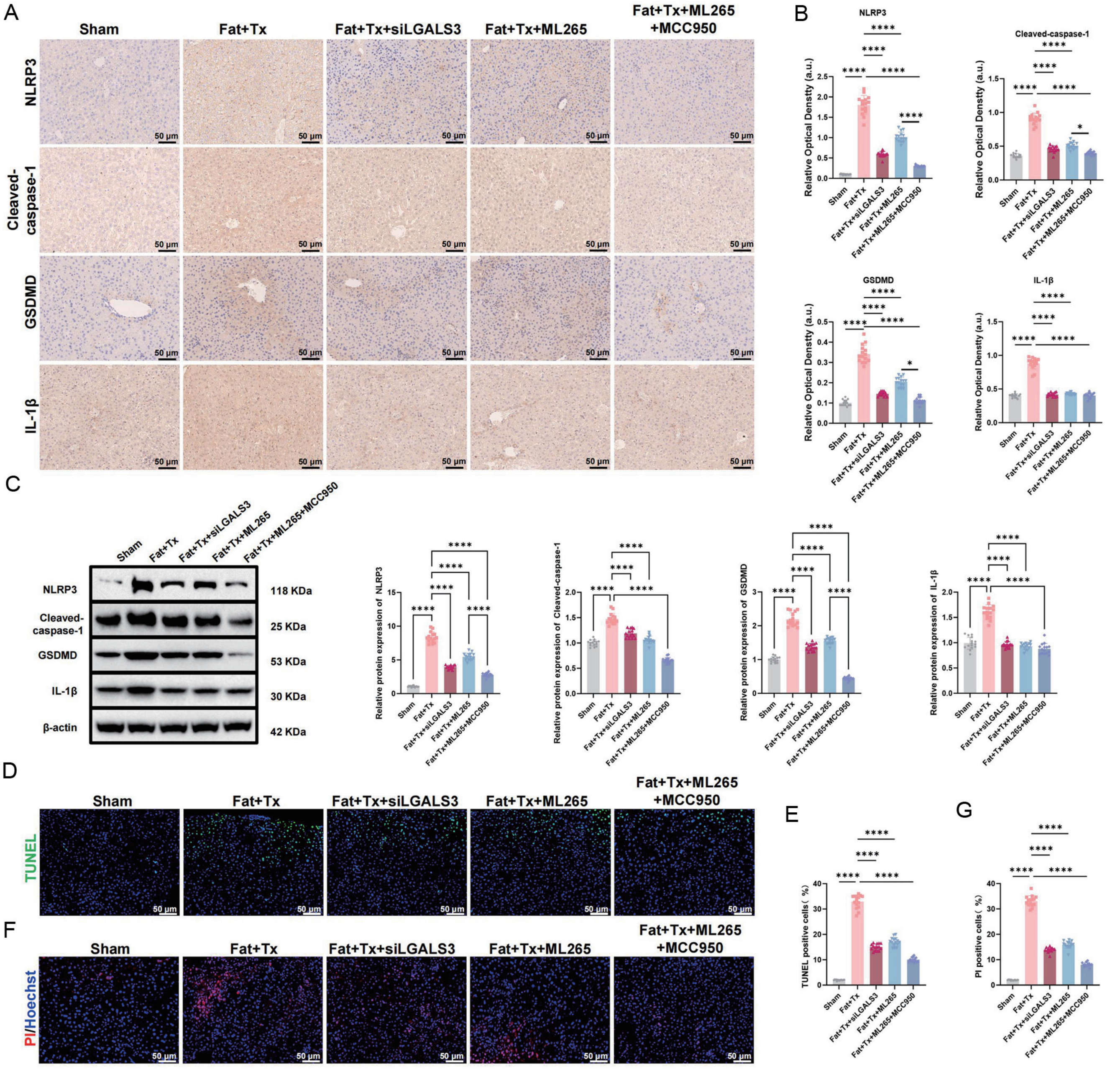

Fig. 6. Assessment of pyroptosis-associated markers and cell death in liver grafts after transplantation. (A) Representative immunohistochemical staining of NLRP3, cleaved caspase-1, GSDMD, and IL-1β in liver grafts. (B) Quantitative analysis of immunohistochemical staining intensity and corresponding mRNA expression levels. (C) Western blot analysis of NLRP3, cleaved caspase-1, GSDMD, and IL-1β expression. (D–E) TUNEL staining of liver tissues and quantification of TUNEL-positive cells (original magnification, 200×). (F) PI/Hoechst double staining of liver tissues. (G) Quantitative analysis of the percentage of PI/Hoechst double-positive cells. Data are presented as mean ± SD (n = 15). $*P < 0.05$, $****P < 0.0001$. TUNEL, terminal deoxynucleotidyl transferase-mediated dUTP nick-end labeling; PI, propidium iodide; SD, standard deviation; mRNA, messenger RNA.

Notably, LGALS3 exhibits a context-dependent dual regulatory role in inflammation. On the one hand, it promotes tissue repair by enhancing macrophage chemotaxis and activating TGF-β signaling; on the other hand, its upregulation can exacerbate inflammatory responses and contribute to tissue injury.[67,68] In the human HepG2-FFA I/R model, we observed that OE-LGALS3 markedly enhanced NLRP3 inflammasome activity and upregulated downstream pyroptosis-associated proteins, including IL-1β and Caspase-1. Conversely, sh-LGALS3 significantly suppressed inflammatory signaling and ROS production, thereby preserving mitochondrial homeostasis. These findings indicate that LGALS3 facilitated pyroptosis and aggravated I/R injury by forming a positive feedback loop through the ROS-NLRP3 signaling axis.

In this study, LGALS3 was silenced using siRNA, and ML265 (an LGALS3-related inhibitor), together with MCC950 (a selective NLRP3 inhibitor), were employed as pharmacological interventions to validate the critical roles of LGALS3

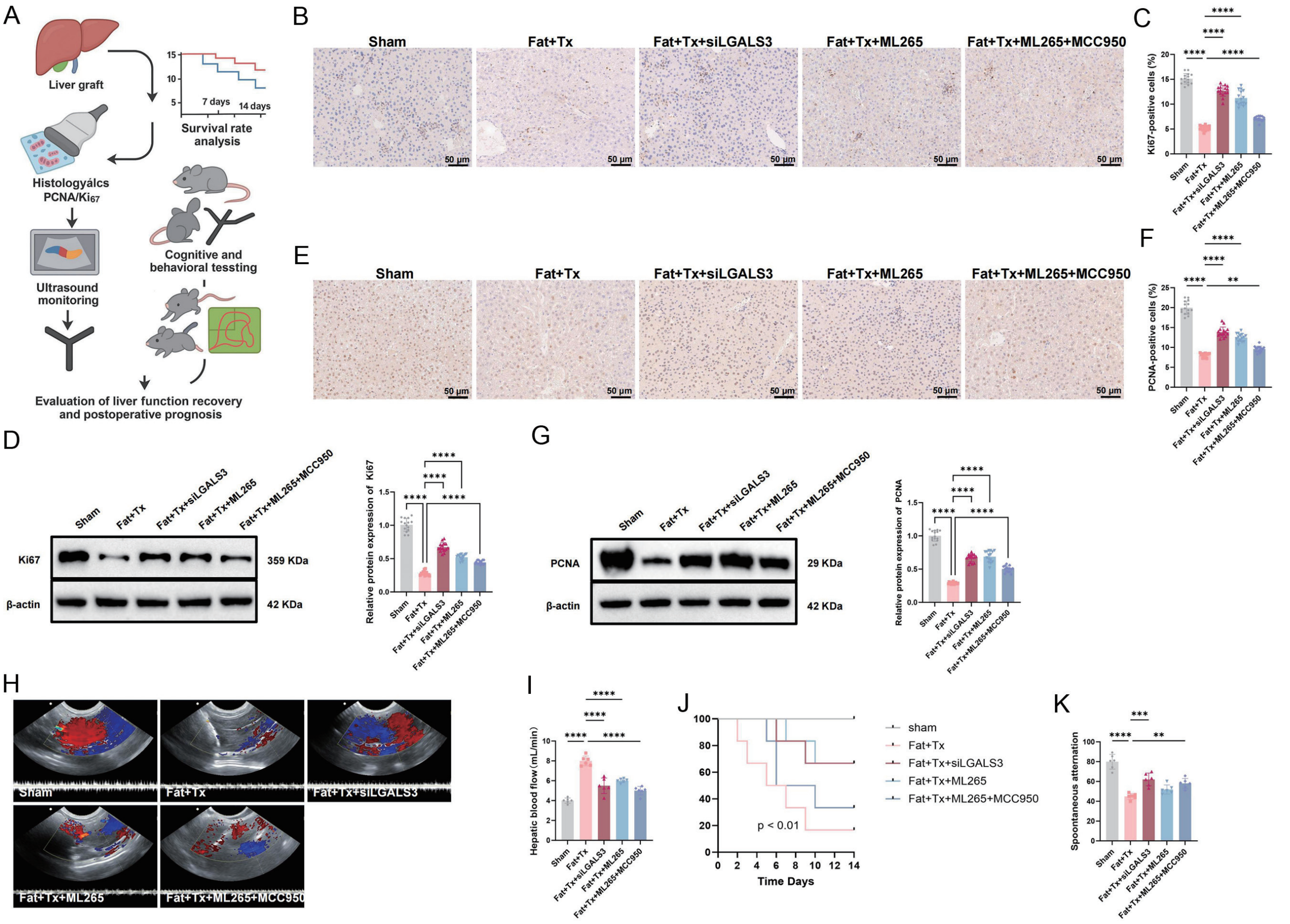

Fig. 7. Assessment of liver regeneration, hemodynamic parameters, and survival after transplantation. (A) Experimental timeline for postoperative functional assessment. (B, E) Immunohistochemical staining of Ki67 in liver tissues and quantification of Ki67-positive cells. (C, F) Immunohistochemical staining of PCNA and corresponding quantitative analysis. (D, G) Western blot analysis of Ki67 and PCNA expression. (H–I) Doppler ultrasound analysis of portal vein flow velocity and hepatic artery resistance index. (J) Kaplan–Meier survival curves of recipient mice over a 14-day observation period. (K) Y-maze test assessing spontaneous alternation behavior. Data are presented as mean ± SD. Survival differences were analyzed using the log-rank test. Ki67, marker of proliferation Ki-67; PCNA, proliferating cell nuclear antigen; SD, standard deviation; Y-maze, Y-shaped maze behavioral test.

and NLRP3 in steatotic liver transplantation. Mechanistically, LGALS3 maintains PKM2 at a high protein level by inhibiting PKM2 degradation, whereas ML265 is a specific activator of PKM2. LGALS3 expression is highly dependent on the inflammatory microenvironment, and activation of PKM2 by ML265 suppresses the release of inflammatory mediators, thereby indirectly reducing the inducible expression of LGALS3.[69,70] Thus, ML265 is not a direct LGALS3 inhibitor but rather an indirect suppressor of LGALS3 expression via PKM2 activation. In parallel, MCC950 was used as a comparator intervention. Multiple studies have demonstrated that MCC950 is a selective inhibitor of the NLRP3 inflammasome, capable of effectively blocking NLRP3 activation under inflammatory conditions both *in vivo* and *in vitro*, and consequently reducing downstream IL-1β production.[71,72] Accordingly, the combined use of ML265 and MCC950 enabled targeted modulation of the LGALS3-PKM2 axis and the NLRP3 inflammasome, providing mechanistic validation of their roles in post-transplant injury of steatotic liver grafts.

Notably, our experimental results revealed a phenomenon in which ML265 or MCC950 alone significantly promoted hepatocyte regeneration, whereas their combined administration resulted in an attenuated effect. The role of NLRP3 in liver regeneration remains controversial. Some studies have reported that inhibition of NLRP3 inflammasome activation enhances liver regeneration in acute liver failure,[73] whereas others have shown that complete genetic deletion of NLRP3 impairs liver regenerative capacity in mice.[74] Emerging evidence suggests that NLRP3 regulates not only IL-1β but also IL-18 expression, and IL-18 has been shown to promote the proliferation of normal human hepatocytes (LO-2 cells).[75] Based on these findings, we speculate that although combined ML265 and MCC950 treatment effectively suppresses inflammatory cytokine production, it may simultaneously disrupt NLRP3-dependent signaling pathways that are essential for liver regeneration, thereby failing to further enhance regenerative capacity. This effect may be partly mediated by altered IL-18 signaling, although additional mechanistic studies are required to validate this hypothesis.

Furthermore, through a series of *in vitro* and *in vivo* experiments, this study is the first to uncover a novel mechanism by which LGALS3 regulates NLRP3 ubiquitination. In the OE-LGALS3 group, the level of NLRP3 ubiquitination was significantly reduced, suggesting that LGALS3 may inhibit ubiquitin-mediated degradation of NLRP3, thereby prolonging its half-life and enhancing its activity. In contrast, shLGALS3 increased NLRP3 ubiquitination levels, limiting excessive inflammasome activation. By constructing a site-specific NLRP3 ubiquitination mutant, we further confirmed that this modification site was essential for NLRP3 function; the mutant lost its ability to activate pyroptotic signaling under OE-LGALS3. This discovery expanded our understanding of NLRP3 regulatory mechanisms and highlighted a novel direction for targeting NLRP3 through its ubiquitination status. Using the MusiteDeep database, we predicted ubiquitination sites on the NLRP3 protein and identified five high-confidence candidate lysine residues (corresponding to Fig. 3C). Among these candidates, the K192 residue was selected for site-directed mutagenesis based on the following considerations. First, K192 exhibited the highest PTM score (0.631) among all predicted sites, indicating a substantially higher probability of ubiquitination compared with the other candidates. Second, integrating our experimental findings with current knowledge in the field, we consider K192 not to be the sole ubiquitination site of NLRP3 but rather a key site specifically regulated by LGALS3. Consistent with this notion, mutational analysis revealed that LGALS3 overexpression-induced ubiquitination of NLRP3 was significantly reduced, but not completely abolished, in the K192 mutant compared with the wild-type protein (Fig. 3B). This observation indirectly suggests that additional lysine residues may contribute to the basal ubiquitination of NLRP3, whereas ubiquitination at K192 is selectively modulated by LGALS3. As a central regulator of inflammatory responses, NLRP3 activity is known to be finely controlled through multiple modification sites and signaling pathways rather than a single regulatory node.[27] From an evolutionary perspective, a regulatory architecture characterized by one core regulatory site accompanied by multiple auxiliary sites is more consistent with the requirements of biological robustness. In this context, K192 may serve as the principal LGALS3-responsive ubiquitination site, ensuring pathway specificity, while the presence of additional ubiquitination sites prevents complete functional inactivation of NLRP3 upon mutation of a single residue, thereby preserving basal inflammatory responsiveness. Although the present study is limited by the lack of mutational validation for all high-scoring candidate sites, the selection of K192 was guided by a three-tiered rationale encompassing prediction confidence, structure-function relevance, and supporting evidence from prior studies. This strategy was sufficient to elucidate the core mechanism by which LGALS3 regulates NLRP3 ubiquitination.

In a murine model of steatotic liver transplantation, LGALS3 was inhibited using siRNA-mediated knockdown or the small-molecule inhibitor ML265. Both interventions markedly improved graft function, as evidenced by reduced serum levels of ALT, AST, and Tbil, attenuation of inflammatory and fibrotic responses, and significant suppression of hepatic expression of pyroptosis-associated proteins, including NLRP3, caspase-1, and GSDMD. In addition, co-administration of the NLRP3 inhibitor MCC950 further enhanced the anti-inflammatory effect, as reflected by a pronounced decrease in IL-1β and IL-18 levels, suggesting a synergistic benefit from dual-targeted inhibition. However, we also observed that the combined treatment was slightly less effective than ML265 monotherapy in promoting hepatocyte regeneration and maintaining hemodynamic stability, indicating that excessive suppression of inflammatory signaling may impair graft regeneration. This phenomenon warrants further investigation.

The novelty of this study lies in the establishment of a new mechanistic model for post-transplant pyroptosis activation in steatotic liver grafts. We demonstrate that LGALS3 modulates inflammasome activity by regulating the ubiquitination of NLRP3 and, for the first time, propose dual targeting of the LGALS3/NLRP3 axis as a potential therapeutic strategy to improve the prognosis of steatotic liver grafts. This conceptual model advances the understanding of the immunometabolic regulatory network following liver transplantation and provides a theoretical basis for the development of optimized, mechanism-driven clinical intervention strategies.

The experimental design combined HFD-induced hepatic steatosis with Kamada's semi-orthotopic liver transplantation model, thereby accurately recapitulating the core pathological features of clinical steatotic donor liver transplantation. Specifically, a 12-week HFD was used to establish a steatosis model closely resembling human NAFLD, while standardized microsurgical vascular anastomosis techniques were applied to simulate post-transplant I/R injury. This integrated *in vivo* model is highly consistent with the central aim of investigating post-transplant pyroptosis in steatotic liver grafts, providing a clinically relevant physiological context for mechanistic exploration.[76,77] In addition, with regard to the choice of cellular models, HepG2 cells were selected as a widely used and well-characterized hepatocyte-derived cell line. HepG2 cells offer several advantages, including ease of steatosis induction, retention of key hepatocellular functions, high amenability to genetic manipulation, and stable culture with relatively low cost. Consequently, they are frequently employed in studies investigating the molecular mechanisms of NAFLD.[31] These characteristics make HepG2 cells suitable for addressing the fundamental mechanistic questions related to LGALS3 in steatotic liver graft injury, thereby fulfilling the requirements of the present study's *in vitro* experiments.[78]

Although this study elucidated the critical role of LGALS3 in steatotic liver graft injury, several limitations remain. First, the BALB/c mouse model of liver injury used in this study, while capable of reproducing the core pathological features of liver disease, cannot fully recapitulate the complex microenvironment of human disease nor the substantial inter-individual heterogeneity observed in clinical patients. These differences may introduce bias when translating the findings to clinical settings. Second, in the *in vitro* experiments, HepG2 cells were employed as a hepatocyte model. However, HepG2 cells harbor TERT promoter mutations and chromosomal abnormalities, resulting in altered cell-cycle regulation and apoptosis/pyroptosis signaling pathways compared with normal hepatocytes.[78] Moreover, their phase I/II metabolic enzyme activities are markedly lower than those of primary human hepatocytes.[79] In addition, monoculture systems cannot simulate key post-transplant processes such as cell–cell communication, vascular regeneration, and immune cell infiltration. Consequently, reliance on HepG2 cells alone may lead to discrepancies between *in vitro* drug sensitivity and the true *in vivo* or clinical context, limiting the extent to which the observed LGALS3–NLRP3 signaling axis can fully mirror the *in vivo* pathological state. Third, regarding the choice of small-molecule and genetic interventions, siRNA-based approaches face substantial translational challenges. The stability of siRNA-lipid nanoparticle formulations remains a major hurdle, and unresolved issues related to immunogenicity and toxicity continue to impede clinical application.[80] Thus, comprehensive preclinical drug-drug interaction and safety studies are required before clinical translation. At present, LGALS3 inhibitors and related small-molecule compounds remain largely confined to preclinical research, and their pharmacokinetic and pharmacodynamic properties have not yet been validated in clinical trials. In this study, LGALS3 inhibitors were administered intraperitoneally to recipient mice one day before surgery and 6 h after transplantation. Through molecular and functional analyses, we demonstrated that LGALS3 acts as an upstream regulator of the NLRP3–IL-1β–NF-κB axis, modulating post-transplant pyroptosis and thereby influencing functional recovery of steatotic liver grafts. Based on these findings, we speculate that targeted LGALS3 therapy administered before and after transplantation may be a feasible strategy in future clinical studies. However, the optimal timing, dosage, and frequency of administration remain to be determined and warrant further investigation. Finally, with respect to drug delivery strategies, our animal experiments confirmed that intraperitoneal administration of LGALS3 inhibitors achieves favorable therapeutic effects. Advances in nanocarrier- and vesicle-based drug delivery systems offer promising opportunities to enable targeted delivery and prolonged drug retention. Accordingly, future studies will focus on engineering optimized delivery systems for LGALS3 inhibitors, along with rigorous evaluation of their safety, stability, and therapeutic efficacy, to facilitate eventual clinical translation.

Future studies may benefit from employing cell models that more closely reflect physiological conditions, such as HepaRG cells or primary human hepatocytes, to systematically evaluate the consistency of LGALS3-mediated regulation of pyroptosis across different cellular contexts. In addition, the integration of three-dimensional (3D) culture systems, including spheroid co-culture models composed of HepG2 cells and liver sinusoidal endothelial cells, would enable simulation of the native hepatic architecture and intercellular interactions, thereby facilitating assessment of how the microenvironment modulates the LGALS3–NLRP3 signaling axis.[27,39] Moreover, further validation using clinical specimens, in combination with hepatic organoid models and spatial transcriptomics technologies, will be essential to strengthen the translational relevance of these findings and to more comprehensively elucidate the spatial and cellular dynamics of LGALS3–NLRP3-mediated regulation in steatotic liver graft injury. Additionally, future studies integrating patient cohort analyses, organoid-based modeling, and spatial transcriptomics will be essential for further validating these findings and enabling the development of more precise therapeutic strategies. These approaches may facilitate the translation of these mechanistic insights into effective clinical interventions for managing complications associated with steatotic donor liver transplantation.

Conclusions

This study systematically demonstrated that LGALS3 promotes inflammasome activation and pyroptosis after steatotic liver transplantation by regulating the ubiquitination of NLRP3, thereby exacerbating graft injury. Targeted inhibition of LGALS3 and its downstream NLRP3 signaling axis significantly improved liver function and survival outcomes in steatotic liver transplantation models. These findings not only expand our understanding of the molecular mechanisms underlying complications in steatotic liver transplantation but also provide a theoretical and experimental basis for developing novel anti-pyroptotic therapies, with substantial scientific and clinical implications for liver transplantation and other I/R-associated liver diseases.

Funding

This study was supported by the Science and Technology Plan Project of the Guizhou Provincial Science and Technology Department (No. QKHJC-zk[2022]-General 418).

Conflict of interest

The authors have no conflict of interests related to this publication.

Author contributions

Experiment design and performance, data analysis, drafting of the manuscript (XY, SH, RM), animal models, sample collection, histological analyses (ZZ, YZ), *in vitro* experiments, data interpretation (JY), study conception, study supervision, funding acquisition, and critical revision of the manuscript (HG, JD). All authors reviewed and approved the final manuscript and agree to be accountable for all aspects of the work.

Ethical statement

All animal experiments were approved by the Animal Ethics Committee of the Affiliated Hospital of Guizhou Medical University (2024-729). The use of human liver samples was approved by the Ethics Committee of the Affiliated Hospital of Guizhou Medical University (2022-52). All procedures conformed to the principles of the Declaration of Helsinki (as revised in 2024) and relevant national regulations. Written informed consent was obtained from all organ donors or their legal representatives prior to sample collection. All animals received human care.

Data sharing statement

All data generated or analyzed during this study are included in this article and/or its supplementary material files. Further inquiries can be directed to the corresponding author.

References

[1] Rinella ME, Neuschwander-Tetri BA, Siddiqui MS, Abdelmalek MF, Caldwell S, Barb D, *et al*. AASLD Practice Guidance on the clinical assessment and management of nonalcoholic fatty liver disease. Hepatology 2023;77(5):1797–1835. doi:10.1097/HEP.0000000000000323, PMID:36727674.

[2] Younossi ZM, Golabi P, Paik JM, Henry A, Van Dongen C, Henry L. The global epidemiology of nonalcoholic fatty liver disease (NAFLD) and nonalcoholic steatohepatitis (NASH): a systematic review. Hepatology 2023;77(4):1335–1347. doi:10.1097/HEP.0000000000000004, PMID:36626630.

[3] Mao Y, Du J, Li B, Wang J, Xuan S, Yang S, *et al*. Global burden of NAFLD 1990-2021 and projections to 2035: Results from the Global Burden of Disease study 2021. PLoS One 2025;20(8):e0330504. doi:10.1371/journal.pone.0330504, PMID:40845036.

[4] Gu Y, Guo C, Liu Z, Zhang Y, Han X, Zhang X, *et al*. The trend in incidence of non-alcoholic fatty liver disease and its impact on cirrhosis and liver cancer: An analysis from Global Burden of Disease 2021. Public Health 2025;242:79–86. doi:10.1016/j.puhe.2025.02.028, PMID:40037155.

[5] Younossi ZM. Non-alcoholic fatty liver disease - A global public health perspective. J Hepatol 2019;70(3):531–544. doi:10.1016/j.jhep.2018.10.033, PMID:30414863.

[6] Lonardo A, Mantovani A, Petta S, Carraro A, Byrne CD, Targher G. Metabolic mechanisms for and treatment of NAFLD or NASH occurring after liver transplantation. Nat Rev Endocrinol 2022;18(10):638–650. doi:10.1038/s41574-022-00711-5, PMID:35840803.

[7] Shi S, Zhu C, Shi S, Li X, Muhammad I, Xu Q, *et al*. Human spindle-shaped urine-derived stem cell exosomes alleviate severe fatty liver ischemia-reperfusion injury by inhibiting ferroptosis via GPX4. Stem Cell Res Ther 2025;16(1):81. doi:10.1186/s13287-025-04202-y, PMID:39985001.

[8] Yang L, Li W, Huang Z, Zhao Y, Sun Z, Wang H, *et al*. Engineered Macrophage Membrane-Coated Nanoparticles for Hepatic Ischemia-Reperfusion Injury Therapeutics. Biomater Res 2025;29:0212. doi:10.34133/bmr.0212, PMID:40416938.

[9] Abbas SH, Ceresa CDL, Pollok JM. Steatotic Donor Transplant Livers: Preservation Strategies to Mitigate against Ischaemia-Reperfusion Injury. Int J Mol Sci 2024;25(9):4648. doi:10.3390/ijms25094648, PMID:38731866.

[10] Huang W, Meng W, Zhao J, Zhang B. Sterile Inflammation and Cell Death Pathways in Liver Ischemia-Reperfusion Injury: A Review and Perspective. Endocr Metab Immune Disord Drug Targets 2025;26:e18715303401342. doi:10.2174/0118715303401342250514102731, PMID:40396312.

[11] Baidya R, Gautheron J, Crawford DHG, Wang H, Bridle KR. Inhibition of MLKL Attenuates Necroptotic Cell Death in a Murine Cell Model of Ischaemia Injury. J Clin Med 2021;10(2):212. doi:10.3390/jcm10020212, PMID:33435617.

[12] Lucas-Ruiz F, Peñín-Franch A, Pons JA, Ramírez P, Pelegrín P, Cuevas S, *et*

al. Emerging Role of NLRP3 Inflammasome and Pyroptosis in Liver Transplantation. Int J Mol Sci 2022;23(22):14396. doi:10.3390/ijms232214396, PMID:36430874.

[13] Shi Y, Hu Y, Li J, Chen H, Zhong Q, Ma X, *et al*. Inhibition of Caspase-1 Suppresses GSDMD-mediated Peritoneal Mesothelial Cell Pyroptosis and Inflammation in Peritoneal Fibrosis. Small 2025;21(14):e2409362. doi:10.1002/smll.202409362, PMID:40018871.

[14] Shang DF, Xu WQ, Zhao Q, Zhao CL, Wang SY, Han YL, *et al*. Molecular mechanisms of pyroptosis in non-alcoholic steatohepatitis and feasible diagnosis and treatment strategies. Pharmacol Res 2025;216:107754. doi:10.1016/j.phrs.2025.107754, PMID:40306603.

[15] Paget C, Doz-Deblauwe E, Winter N, Briard B. Specific NLRP3 Inflammasome Assembling and Regulation in Neutrophils: Relevance in Inflammatory and Infectious Diseases. Cells 2022;11(7):1188. doi:10.3390/cells11071188, PMID:35406754.

[16] de Carvalho Ribeiro M, Szabo G. Role of the Inflammasome in Liver Disease. Annu Rev Pathol 2022;17:345–365. doi:10.1146/annurev-pathmechdis-032521-102529, PMID:34752711.

[17] Zhu S, Liao L, Zhong Y, Liu Z, Lu J, Yang Z, *et al*. Hepatocellular CMPK2 promotes the development of metabolic dysfunction-associated steatohepatitis. J Hepatol 2025;83(2):383–396. doi:10.1016/j.jhep.2025.01.008, PMID:39855350.

[18] Fang Y, Liu X, Liu Y, Xu N. Insights into the Mode and Mechanism of Interactions Between RNA and RNA-Binding Proteins. Int J Mol Sci 2024;25(21):11337. doi:10.3390/ijms252111337, PMID:39518890.

[19] García-Moreno JF, Romão L. Perspective in Alternative Splicing Coupled to Nonsense-Mediated mRNA Decay. Int J Mol Sci 2020;21(24):9424. doi:10.3390/ijms21249424, PMID:33321981.

[20] Wang X, Li J, Zhang C, Guan X, Li X, Jia W, *et al*. Old players and new insights: unraveling the role of RNA-binding proteins in brain tumors. Theranostics 2025;15(11):5238–5257. doi:10.7150/thno.113312, PMID:40303323.

[21] Goswami B, Nag S, Ray PS. Fates and functions of RNA-binding proteins under stress. Wiley Interdiscip Rev RNA 2024;15(1):e1825. doi:10.1002/wrna.1825, PMID:38014833.

[22] Sun MJ, Cao ZQ, Leng P. The roles of galectins in hepatic diseases. J Mol Histol 2020;51(5):473–484. doi:10.1007/s10735-020-09898-1, PMID:32734557.

[23] Arsenijevic A, Stojanovic B, Milovanovic J, Arsenijevic D, Arsenijevic N, Milovanovic M. Galectin-3 in Inflammasome Activation and Primary Biliary Cholangitis Development. Int J Mol Sci 2020;21(14):5097. doi:10.3390/ijms21145097, PMID:32707678.

[24] Liu Z, Wang B, Li S, Zhao C, Dai W, Huang Z, *et al*. Oral Administration of a Tetrahedral Framework DNA-Based Nanoshot Attenuates Liver Fibrosis via Targeting Galectin-3. ACS Nano 2025;19(26):23876–23892. doi:10.1021/acsnano.5c05144, PMID:40556451.

[25] Lee YJ, Song YK. Cooperative interaction between interleukin 10 and galectin-3 against liver ischemia-reperfusion injury. Clin Cancer Res 2002;8(1):217–220. PMID:11801562.

[26] Sotoudeheian M. Galectin-3 and Severity of Liver Fibrosis in Metabolic Dysfunction-Associated Fatty Liver Disease. Protein Pept Lett 2024;31(4):290–304. doi:10.2174/0109298665301698240404061300, PMID:38715329.

[27] Chen Y, Jiang Q, Xing X, Xu L, Zhao Q, Zhang Q, *et al*. Macrophage Derived Galectin-3 Promotes Renal Fibrosis and Diabetic Kidney Disease by Enhancing TGFβ1 Signaling. Adv Sci (Weinh) 2025;12(35):e04032. doi:10.1002/advs.202504032, PMID:40799164.

[28] Zhou X, Yang X, Huang S, Lin G, Lei K, Wang Q, *et al*. Inhibition of METTL3 Alleviates NLRP3 Inflammasome Activation via Increasing Ubiquitination of NEK7. Adv Sci (Weinh) 2024;11(26):e2308786. doi:10.1002/advs.202308786, PMID:38696610.

[29] Chen Y, Liu Y, Jiang K, Wen Z, Cao X, Wu S. Linear ubiquitination of LKB1 activates AMPK pathway to inhibit NLRP3 inflammasome response and reduce chondrocyte pyroptosis in osteoarthritis. J Orthop Translat 2023;39:1–11. doi:10.1016/j.jot.2022.11.002, PMID:36514784.

[30] Li H, Xiao L, He H, Zeng H, Liu J, Jiang C, *et al*. Quercetin Attenuates Atherosclerotic Inflammation by Inhibiting Galectin-3-NLRP3 Signaling Pathway. Mol Nutr Food Res 2021;65(15):e2000746. doi:10.1002/mnfr.202000746, PMID:33939881.

[31] Li H, Cao Z, Wang L, Li J, Cheng X, Tang Y, *et al*. Chronic high-fat diet induces galectin-3 and TLR4 to activate NLRP3 inflammasome in NASH. J Nutr Biochem 2023;112:109217. doi:10.1016/j.jnutbio.2022.109217, PMID:36402251.

[32] Zhou M, Hui J, Gao L, Liang J, Wang C, Xu J. Extracellular vesicles from bone marrow mesenchymal stem cells alleviate acute rejection injury after liver transplantation by carrying miR-22-3p and inducing M2 polarization of Kupffer cells. J Gene Med 2023;25(7):e3497. doi:10.1002/jgm.3497, PMID:36890611.

[33] Maseko TE, Elkalaf M, Peterová E, Lotková H, Staňková P, Melek J, *et al*. Comparison of HepaRG and HepG2 cell lines to model mitochondrial respiratory adaptations in non-alcoholic fatty liver disease. Int J Mol Med 2024;53(2):18. doi:10.3892/ijmm.2023.5342, PMID:38186319.

[34] Li B, Xia C, He W, Liu J, Duan R, Ji Z, *et al*. The Thyroid Hormone Analog GC-1 Mitigates Acute Lung Injury by Inhibiting M1 Macrophage Polarization. Adv Sci (Weinh) 2024;11(44):e2401931. doi:10.1002/advs.202401931, PMID:39373388.

[35] Luo L, Wang F, Xu X, Ma M, Kuang G, Zhang Y, *et al*. STAT3 promotes NLRP3 inflammasome activation by mediating NLRP3 mitochondrial translocation. Exp Mol Med 2024;56(9):1980–1990. doi:10.1038/s12276-024-01298-9, PMID:39218978.

[36] Nair VD, McNaught KS, González-Maeso J, Sealfon SC, Olanow CW. p53 mediates nontranscriptional cell death in dopaminergic cells in response to proteasome inhibition. J Biol Chem 2006;281(51):39550–39560. doi:10.1074/jbc.M603950200, PMID:17060322.

[37] Chen B, Li H, Ou G, Ren L, Yang X, Zeng M. Curcumin attenuates MSU crystal-induced inflammation by inhibiting the degradation of IκBα and blocking mitochondrial damage. Arthritis Res Ther 2019;21(1):193. doi:10.1186/s13075-019-1974-z, PMID:31455356.

[38] Nasiri-Ansari N, Nikolopoulou C, Papoutsi K, Kyrou I, Mantzoros CS, Kyriakopoulos G, *et al*. Empagliflozin Attenuates Non-Alcoholic Fatty Liver Disease (NAFLD) in High Fat Diet Fed ApoE$^{(-/-)}$ Mice by Activating Autophagy and Reducing ER Stress and Apoptosis. Int J Mol Sci 2021;22(2):E818. doi:10.3390/ijms22020818, PMID:33467546.

[39] Bai C, Xiao P, Chen Y, Chu F, Jiao Y, Fan J, *et al*. GPX4 Promoter Hypermethylation Induced by Ischemia/Reperfusion Injury Regulates Hepatocytic Ferroptosis. J Clin Transl Hepatol 2024;12(11):917–929. doi:10.14218/JCTH.2024.00135, PMID:39544244.

[40] Sun P, Zhang P, Wang PX, Zhu LH, Du Y, Tian S, *et al*. Mindin deficiency protects the liver against ischemia/reperfusion injury. J Hepatol 2015;63(5):1198–1211. doi:10.1016/j.jhep.2015.06.033, PMID:26165142.

[41] Dong X, Nie J, Huang A, Chen L, Zang E, Xiang Z, *et al*. A novel small molecule NJH-13 induces pyroptosis via the Ca(2+) driven AKT-FOXO1-GSDME signaling pathway in NSCLC by targeting TRPV5. J Adv Res 2025;77:733–746. doi:10.1016/j.jare.2025.01.028, PMID:39832720.

[42] Li X, Wang D, Yang C, Zhou Q, Zhuoga SL, Wang LQ, *et al*. Establishment of age- and gender-specific pediatric reference intervals for liver function tests in healthy Han children. World J Pediatr 2018;14(2):151–159. doi:10.1007/s12519-018-0126-x, PMID:29546581.

[43] Aboseif A, Mangioris G, Yang B, Pazdernik VK, Britton JW, Dubey D, *et al*. Cytokine, Chemokine, and Neurofilament Light Chain Signatures in LGI1 Autoimmune Encephalitis. Ann Clin Transl Neurol 2025;12(11):2258–2270. doi:10.1002/acn3.70158, PMID:40781580.

[44] Wang D, Liu D, Yuchi J, He F, Jiang Y, Cai S, *et al*. MusiteDeep: a deep-learning based webserver for protein post-translational modification site prediction and visualization. Nucleic Acids Res 2020;48(W1):W140–W146. doi:10.1093/nar/gkaa275, PMID:32324217.

[45] Lan T, Hu Y, Hu F, Li H, Chen Y, Zhang J, *et al*. Hepatocyte glutathione S-transferase mu 2 prevents non-alcoholic steatohepatitis by suppressing ASK1 signaling. J Hepatol 2022;76(2):407–419. doi:10.1016/j.jhep.2021.09.040, PMID:34656650.

[46] Chen J, Jin H, Zhou H, Hei X, Liu K. Research into the characteristic molecules significantly affecting liver cancer immunotherapy. Front Immunol 2023;14:1029427. doi:10.3389/fimmu.2023.1029427, PMID:36860864.

[47] Li R, Xue W, Wei H, Fan Q, Li X, Qiu Y, *et al*. Research Progress of Pyroptosis in Fatty Liver Disease. Int J Mol Sci 2023;24(17):13065. doi:10.3390/ijms241713065, PMID:37685870.

[48] Xu Z, Tang C, Song X, Liu Z, Zhou J, Shi Q, *et al*. High uric acid exacerbates nonalcoholic steatohepatitis through NLRP3 inflammasome and gasdermin D-mediated pyroptosis. J Biol Chem 2025;301(6):110249. doi:10.1016/j.jbc.2025.110249, PMID:40398602.

[49] Subramanian P, Chavakis T. The complex function of macrophages and their subpopulations in metabolic injury associated fatty liver disease. J Physiol 2023;601(7):1159–1171. doi:10.1113/JP283820, PMID:36825510.

[50] You W, Berendschot TTJM, Knoops K, van Zandvoort MAMJ, Webers CAB, Reutelingsperger CPM, *et al*. Single Cell Analysis of Reversibility of the Cell Death Program in Ethanol-Treated Neuronal PC12 Cells. Int J Mol Sci 2022;23(5):2650. doi:10.3390/ijms23052650, PMID:35269792.

[51] Yang M, Shu W, Zhai X, Yang X, Zhou H, Pan B, *et al*. Integrated multi-omic analysis identifies fatty acid binding protein 4 as a biomarker and therapeutic target of ischemia-reperfusion injury in steatotic liver transplantation. Cell Mol Life Sci 2024;81(1):83. doi:10.1007/s00018-023-05110-1, PMID:38341383.

[52] Liu H, Zhu Y, Ng KT, Lo CM, Man K. The Landscape of Aberrant Alternative Splicing Events in Steatotic Liver Graft Post Transplantation via Transcriptome-Wide Analysis. Int J Mol Sci 2023;24(9):8216. doi:10.3390/ijms24098216, PMID:37175922.

[53] Yang X, Lu D, Wang R, Lian Z, Lin Z, Zhuo J, *et al*. Single-cell profiling reveals distinct immune phenotypes that contribute to ischaemia-reperfusion injury after steatotic liver transplantation. Cell Prolif 2021;54(10):e13116. doi:10.1111/cpr.13116, PMID:34469018.

[54] Liu R, Cao H, Zhang S, Cai M, Zou T, Wang G, *et al*. ZBP1-mediated apoptosis and inflammation exacerbate steatotic liver ischemia/reperfusion injury. J Clin Invest 2024;134(13):e180451. doi:10.1172/JCI180451, PMID:38743492.

[55] Li X, Yin X, Xu J, Geng L. Application of Steatotic Donor Livers in Liver Transplantation. Korean J Gastroenterol 2025;85(2):160–169. doi:10.4166/kjg.2025.013, PMID:40276834.

[56] Ho NX, Tingle SJ, Kourounis G, Mahendran B, Bramley R, Thompson ER, *et al*. Visual assessment of liver steatosis at retrieval predicts long term liver transplant outcomes in donation following circulatory death. HPB (Oxford) 2025;27(5):630–639. doi:10.1016/j.hpb.2025.01.007, PMID:39920010.

[57] Bardallo RG, Chullo G, Alva N, Rosello-Catafau J, Fundora-Suárez Y, Carbonell T, *et al*. Mitigating Cold Ischemic Injury: HTK, UW and IGL-2 Solution's Role in Enhancing Antioxidant Defence and Reducing Inflammation in Steatotic Livers. Int J Mol Sci 2024;25(17):9318. doi:10.3390/ijms25179318, PMID:39273266.

[58] Li T, Chang P, Wang Y, Song Y, Qu P, Wang B, *et al*. HOPE and AMPK activation reduce reperfusion injury and metabolic dysfunction in primate steatotic liver grafts. Sci Rep 2025;15(1):11762. doi:10.1038/s41598-025-96265-3, PMID:40189683.

[59] Makino K, Ishii T, Ogiso S, Nakakura A, Nishio T, Fukumitsu K, *et al*. Combination of risk alleles of PNPLA3, TM6SF2, and HSD17B13 of donors can predict recurrence of steatotic liver disease after liver transplantation. Hepatol Res 2024;54(12):1148–1157. doi:10.1111/hepr.14086, PMID:39031833.

[60] Wang T, Fang Y, Zhang X, Yang Y, Jin L, Li Z, *et al*. Heme Oxygenase-1 Alleviates Ischemia-Reperfusion Injury by Inhibiting Hepatocyte Pyroptosis after Liver Transplantation in Rats. Front Biosci (Landmark Ed) 2023;28(10):275. doi:10.31083/j.fbl2810275, PMID:37919062.
[61] Yu W, Zhang Y, Sun L, Huang W, Li X, Xia N, *et al*. Myeloid Trem2 ameliorates the progression of metabolic dysfunction-associated steatotic liver disease by regulating macrophage pyroptosis and inflammation resolution. Metabolism 2024;155:155911. doi:10.1016/j.metabol.2024.155911, PMID:38609037.
[62] Kram M. Galectin-3 inhibition as a potential therapeutic target in non-alcoholic steatohepatitis liver fibrosis. World J Hepatol 2023;15(2):201–207. doi:10.4254/wjh.v15.i2.201, PMID:36926236.
[63] Tamaki N, Ajmera V, Loomba R. Non-invasive methods for imaging hepatic steatosis and their clinical importance in NAFLD. Nat Rev Endocrinol 2022;18(1):55–66. doi:10.1038/s41574-021-00584-0, PMID:34815553.
[64] Liu H, Yeung WHO, Pang L, Liu J, Liu XB, Pan Ng KT, *et al*. Arachidonic acid activates NLRP3 inflammasome in MDSCs via FATP2 to promote post-transplant tumour recurrence in steatotic liver grafts. JHEP Rep 2023;5(12):100895. doi:10.1016/j.jhepr.2023.100895, PMID:37916155.
[65] Zhang N, Sheng M, Wu M, Zhang X, Ding Y, Lin Y, *et al*. Berberine protects steatotic donor undergoing liver transplantation via inhibiting endoplasmic reticulum stress-mediated reticulophagy. Exp Biol Med (Maywood) 2019; 244(18):1695–1704. doi:10.1177/1535370219878651, PMID:31554427.
[66] Weng J, Wang X, Xu B, Li W. Augmenter of liver regeneration ameliorates ischemia-reperfusion injury in steatotic liver via inhibition of the TLR4/NF-κB pathway. Exp Ther Med 2021;22(2):863. doi:10.3892/etm.2021.10295, PMID:34178136.
[67] Kim DH, Sung M, Park MS, Sun EG, Yoon S, Yoo KH, *et al*. Galectin 3-binding protein (LGALS3BP) depletion attenuates hepatic fibrosis by reducing transforming growth factor-β1 (TGF-β1) availability and inhibits hepatocarcinogenesis. Cancer Commun (Lond) 2024;44(10):1106–1129. doi:10.1002/cac2.12600, PMID:39073023.
[68] Di Gregoli K, Somerville M, Bianco R, Thomas AC, Frankow A, Newby AC, *et al*. Galectin-3 Identifies a Subset of Macrophages With a Potential Beneficial Role in Atherosclerosis. Arterioscler Thromb Vasc Biol 2020;40(6):1491–1509. doi:10.1161/ATVBAHA.120.314252, PMID:32295421.
[69] Wang H, Fan C, Chen X, Zhou W, Guo L, Zhao F, *et al*. Pyruvate Kinase M2 Nuclear Translocation Regulate Ferroptosis-Associated Acute Lung Injury in Cytokine Storm. Inflammation 2024;47(5):1667–1684. doi:10.1007/s10753-024-02000-x, PMID:38483700.
[70] Nan J, Xia C, Zhang J, Xie Y, Shi S, Yang W, *et al*. Gadolinium-ceria hybrid system enables synergistic alleviation of oxidative stress and metabolic thrombo-inflammation for efficient ischemic stroke treatment. Biomaterials 2025;322:123379. doi:10.1016/j.biomaterials.2025.123379, PMID:40318605.
[71] Li S, Withaar C, Rodrigues PG, Zijlstra SN, de Boer RA, Silljé HHW, *et al*. The NLRP3-inflammasome inhibitor MCC950 improves cardiac function in a HFpEF mouse model. Biomed Pharmacother 2024;181:117711. doi:10.1016/j.biopha.2024.117711, PMID:39616735.
[72] Li H, Guan Y, Liang B, Ding P, Hou X, Wei W, *et al*. Therapeutic potential of MCC950, a specific inhibitor of NLRP3 inflammasome. Eur J Pharmacol 2022;928:175091. doi:10.1016/j.ejphar.2022.175091, PMID:35714692.
[73] Zhan C, Lin G, Huang Y, Wang Z, Zeng F, Wu S. A dopamine-precursor-based nanoprodrug for in-situ drug release and treatment of acute liver failure by inhibiting NLRP3 inflammasome and facilitating liver regeneration. Biomaterials 2021;268:120573. doi:10.1016/j.biomaterials.2020.120573, PMID:33260093.
[74] Ando T, Ito H, Kanbe A, Hara A, Seishima M. Deficiency of NALP3 Signaling Impairs Liver Regeneration After Partial Hepatectomy. Inflammation 2017;40(5):1717–1725. doi:10.1007/s10753-017-0613-6, PMID:28656530.
[75] Shi L, Zhang S, Huang Z, Hu F, Zhang T, Wei M, *et al*. Baicalin promotes liver regeneration after acetaminophen-induced liver injury by inducing NLRP3 inflammasome activation. Free Radic Biol Med 2020;160:163–177. doi:10.1016/j.freeradbiomed.2020.05.012, PMID:32682928.
[76] Radhakrishnan S, Yeung SF, Ke JY, Antunes MM, Pellizzon MA. Considerations When Choosing High-Fat, High-Fructose, and High-Cholesterol Diets to Induce Experimental Nonalcoholic Fatty Liver Disease in Laboratory Animal Models. Curr Dev Nutr 2021;5(12):nzab138. doi:10.1093/cdn/nzab138, PMID:34993389.
[77] Kamada N, Calne RY. Orthotopic liver transplantation in the rat. Technique using cuff for portal vein anastomosis and biliary drainage. Transplantation 1979;28(1):47–50. PMID:377595.
[78] Arzumanian VA, Kiseleva OI, Poverennaya EV. The Curious Case of the HepG2 Cell Line: 40 Years of Expertise. Int J Mol Sci 2021;22(23):13135. doi:10.3390/ijms222313135, PMID:34884942.
[79] Nyberg SL, Remmel RP, Mann HJ, Peshwa MV, Hu WS, Cerra FB. Primary hepatocytes outperform Hep G2 cells as the source of biotransformation functions in a bioartificial liver. Ann Surg 1994;220(1):59–67. PMID:8024360.
[80] El Moukhtari SH, Garbayo E, Amundarain A, Pascual-Gil S, Carrasco-León A, Prosper F, *et al*. Lipid nanoparticles for siRNA delivery in cancer treatment. J Control Release 2023;361:130–146. doi:10.1016/j.jconrel.2023.07.054, PMID:37532145.